UNIVERSITÀ DEGLI STUDI DI PADOVA

Dipartimento di Ingegneria Industriale DII

Corso di Laurea Magistrale in Ingegneria Aerospaziale

A numerical study on wall-resolved large-eddy models in compressible channel flow configuration

Relatore Prof. De Vanna Francesco

Correlatore Prof. Picano Francesco

Motton Thomas 1180323

Anno Accademico 2019/2020

Contents

Introduction

Compressible wall-bounded turbulent flows are of major relevance in the aerospace industry and have been extensively studied with both experimental and numerical techniques. They can be described by the Navier-Stokes equations, for which an analytical solution does not exist: a complete description of a turbulent flow, therefore, can only be obtained by numerically solving the equations. During the years, computational fluid dynamics (CFD) has gained importance because of the fast-paced increase and availability of computational power and its main three ways to deal with the Navier-Stokes equations are the direct numerical simulation (DNS), Reynolds-averaged Navier-Stokes method (RANS) and large-eddy simulation (LES).

The DNS method presupposes direct discretisation and resolution of the Navier-Stokes system of equations without a mathematical model for turbulence. As many reports from the 1900s point out ([42], [43], [44], [45]), acceptable DNS of real-life scenarios would have been generally impossible at the time due to the different time- and space-scales simultaneously at play. For this reason, the evolution of the flow had to be studied statistically, through RANS or LES.

After the pioneering work of Reynolds, Prandtl and von Kármán ([46], [50], [51]), the earliest computational approach to these complex flows was the Reynolds-averaged Navier-Stokes (RANS) method, which deals with the mean properties of the fluid. First successfully implemented by Launder and Spalding (1974) [47], the method was still inaccurate because of its severe constraints in terms of grid points positioning [48]. Later improved by a number of other studies, the RANS technique has been the prevalent one until the last decade [49], but it is still not accurate enough to deal with more delicate problems such as stall in turbomachinery and aircraft, atmospheric re-entry, or other situations where there is a strong interaction between turbulent plumes and wall-related phenomena; in these situations of vital importance, detailed flow-field predictions are strictly required.

A LES is intermediate in computational complexity between DNS and RANS. Used originally for weather forecasting [43], it directly computes the larger vortices while employing a mathematical model to represent the smaller energy-containing scales. The strength of a LES is that it requires far less grid points and computational time than a DNS to yield its results, and having a tool which is able to capture and forecast such extremely complex phenomena without introducing a massive computational burden is paramount in order to further advance the knowledge and study possibilities of turbulent flows. Of course, as will be discussed in Section 3, the accuracy provided by this approach is not at the same level as that of a DNS, but the savings in computational time and overall burden could be worth the approximations.

For what concerns wall turbulence, as discussed in Section 2, there was no consensus until recently on the effect of Mach number and fluid compressibility on the typical length scales in wall turbulence. In this respect, Demetriades and Martindale (1983) [50] found the streamwise length scales in a compressible fluid to be about half as in incompressible ones; moreover, Smits et al. (1989) [51] observed that the length scales sensibly decrease with increasing Mach numbers. On the other hand, Spina et al (1994) claimed the exact opposite, as well as Ganapathisubramani et al (2006) [53]. Further studies by Modesti, Bernardini and Pirozzoli ([49], [17]) seem to settle that typical length scales are in fact substantially insensitive to the Mach number.

In this work a numerical approach based on the LES technique has been followed. This was made possible by the development of the Unsteady Robust All-around Navier-StOkes Solver (URANOS), a tool which enables the LES study — as well as DNS — of turbulent compressible flows with the possibility to include immersed bodies and shock waves. The URANOS software was developed by Francesco de Vanna at the Department of Industrial Engineering of the University of Padova.

Since turbulent flows are rather chaotic in their nature and it is not always clear if the fluctuations they present are due to physical reasons or numerical instabilities, all the data obtained from the simulations has been transformed, using the various mathematical tools presented in Section 4, to match an equivalent incompressible flow for which accurate DNS analysis [30] has already been provided. By doing this, flows at different friction Reynolds numbers Re_τ could be compared using a solid common ground.

1 Navier-Stokes Equations

1.1 Standard Navier-Stokes Equations

The majority of aerospace fluxes are compressible and turbulent in nature. In the case of a turbulent flow, particularly a turbulent boundary layer flow, the need for computational fluid dynamics (CFD) arises. Since turbulence is not yet fully understood nor predictable, there is the call for models and approximations. A compressible viscous flow is described by the Navier-Stokes equations, a set of five non-linear equations. The Navier-Stokes equations for a perfect heat-conducting gas that will be used in this work are:

$$\frac{\partial \rho}{\partial t} = -\frac{\partial(\rho u_i)}{\partial x_i} \tag{1.1}$$

$$\frac{\partial(\rho u_i)}{\partial t} = -\frac{\partial(\rho u_i u_j)}{\partial x_j} - \frac{\partial p \delta_{ij}}{\partial x_j} + \frac{\partial \sigma_{ij}}{\partial x_j} \tag{1.2}$$

$$\frac{\partial(\rho E)}{\partial t} = -\frac{\partial(\rho u_j H)}{\partial x_j} + \frac{\partial(\sigma_{ij} u_i)}{\partial x_j} - \frac{\partial q_j}{\partial x_j} \tag{1.3}$$

These represent the conservation of mass, momentum and energy respectively. Here $i = 1, 2, 3$, $H = E + p/\rho$ is the fluid enthalpy; total energy E can be expressed as

$$E = e + \frac{u_i u_i}{2} \tag{1.4}$$

with the second addendum equalling the kinetic energy and e representing the internal energy

$$e = c_v T = \frac{pR}{(\gamma - 1)} \tag{1.5}$$

Finally, σ_{ij} and q_j are the components of the viscous stress tensor resulting from the relative motion between elementary Newtonian fluid volumes (Reynolds stresses), and heat flux vector respectively, prescribed as

$$\sigma_{ij} = \mu \left(\frac{\partial u_i}{\partial x_j} + \frac{\partial u_j}{\partial x_i} - \frac{2}{3} \frac{\partial u_k}{\partial x_k} \delta_{ij} \right) \tag{1.6}$$

$$q_j = -\lambda \frac{\partial T}{\partial x_j} \tag{1.7}$$

where $\lambda = c_p \mu / Pr$ with $Pr = 0.71$ (i.e. air at $T \simeq 273K$). Since it is known that c_p is essentially constant up to $T \simeq 1000K$, the working fluid has been assumed perfect. The resulting system consists of five equations and seven unknown variables (ρ, ρu_i, ρE, p, T) so it has to be completed with two closure equations. The first closure equation chosen was the thermodynamic equation of state for the perfect gases

$$p = \rho R T \tag{1.8}$$

The second closure equation, for the viscosity μ, is Sutherland's law

$$\mu(T) = T^{3/2} \left(\frac{T_0 + S}{T + S} \right) \tag{1.9}$$

where $T_0 = 273.15K$ and $S = 110.4K$, the empirical value for air.

1.2 Non-dimensional Navier-Stokes equations

It is self-evident that the main difference between a compressible boundary layer and an incompressible one is the presence of density fluctuations

$$\rho = \bar{\rho} + \rho' \tag{1.10}$$

where $\bar{\rho}$ is the average density and ρ' the fluctuating value (Reynolds decomposition). All three conservation relations (1.1-1.3) contain the product ρu_i so additional time-averaged quantities are obtained, involving products of fluctuating variables, as seen in (1.10):

$$\overline{\rho u} = \bar{\rho}\bar{u} + \overline{\rho' u'} \tag{1.11}$$

The same, naturally, occurs for the other components of the velocity. Another effect of fluctuating density is the variability of temperature through the equation of state. This has repercussions for other entities such as viscosity μ, specific heat ratio γ, pressure-fixed specific heat c_p and Prandtl number Pr, which all theoretically depend on T. For these reasons, Equation (1.3) is not the byproduct of (1.1) and (1.2) as it was in the incompressible case, but it has to be used alongside the other two, thus increasing the computational complexity of the problem.

In order to treat the compressible boundary layer, the Navier-Stokes equations are non-dimensionalised: as a result, the number of independent parameters is the minimum possible and they will be on the same order of magnitude, relieving CPU stress. Through the Buckingham theorem, a certain number of independent fundamental dimensional groups can be identified. The theorem states

$$N_g = N_p - (N_d + N_r) \tag{1.12}$$

that is, for a phenomenon governed by N_p dimensional parameters, N_d fundamental dimensions and N_r relations, N_g independent fundamental groups can fully describe the system; of course, N_g is the minimum number of unknowns needed to solve the problem. In the present closed system $N_p = 15$ (t_0, L_0, ρ_0, u_0, p_0, T_0, E_0, μ_0, λ_0, R_0, c_{p0}, c_{v0}, e_0, Pr_0, γ_0), $N_d = 4$ (time [s], length [m], mass [kg], temperature [K]), and $N_r = 7$

$$p_0 = \rho_0 R_0 T_0 \qquad \mu_0 = T_0^{3/2}\left(\frac{T_0 + S}{T_0 + S}\right)$$

$$\lambda_0 = \frac{\mu_0 c_{p0}}{Pr_0} \qquad e_0 = c_{v0} T_0$$

$$E_0 = e_0 + \frac{1}{2}u_0^2 \qquad c_{v0} = \frac{R_0}{\gamma_0 - 1} \qquad c_{p0} = \frac{\gamma R_0}{\gamma_0 - 1} \tag{1.13}$$

So, according to (1.12), $N_g = 4$. The choice of the four independent groups among the fifteen available is completely arbitrary. In this work, L_0 is the reference length, ρ_0 the reference density, p_0 the reference pressure and $u_0 = \sqrt{p_0/\rho_0}$ the reference velocity, i.e. the speed of sound without the already non-dimensional $\sqrt{\gamma_0} = \sqrt{c_{p0}/c_{v0}}$. Using these new variables, the remaining variables can be rewritten as

$$x = L_0 x' \qquad u_i = u_0 u_i' \qquad t = \frac{L_0}{u_0}t' \qquad \rho = \rho_0 \rho' \qquad T = T_0 T'$$

$$e = \frac{p_0}{\rho_0}e' \qquad E_{tot} = \frac{p_0}{\rho_0}E_{tot}' \qquad \mu = \mu_0 \mu' \qquad \lambda = \lambda_0 \lambda' \tag{1.14}$$

where apexes indicate non-dimensional quantities. Substituting the newly found groups into Equation (1.1), the non-dimensional mass conservation equation can be found

$$\frac{\partial(\rho_0 \rho')}{\partial(\frac{L_0}{u_0} t')} = -\frac{\partial(\rho_0 \rho' u_0 u'_i)}{\partial(L_0 x'_i)} \tag{1.15}$$

$$\frac{\partial \rho'}{\partial t'} = -\frac{\partial(\rho' u'_i)}{\partial x'_i} \tag{1.16}$$

which is formally identical to its dimensional counterpart. For the momentum conservation

$$\frac{\partial(\rho' u'_i)}{\partial t'} \frac{\rho_0 u_0^2}{L_0} = -\frac{\partial(\rho' u'_i u'_j)}{\partial x'_j} \frac{\rho_0 u_0^2}{L_0} - \frac{\partial p'_i \delta_{ij}}{\partial x'_j} \frac{p_0}{L_0} + \frac{\partial \sigma_{ij}}{\partial x_j} \tag{1.17}$$

where

$$\frac{\partial \sigma_{ij}}{\partial x_j} = \frac{\partial}{\partial x'_j} \left(\mu' \left(\frac{\partial u'_i}{\partial x'_j} + \frac{\partial u'_j}{\partial x'_i} - \frac{2}{3} \frac{\partial u'_k}{\partial x'_k} \delta_{ij} \right) \right) \frac{\mu_0 u_0}{L_0^2} \tag{1.18}$$

After dividing by $\rho_0 u_0^2 / L_0$ Equation (1.2) becomes

$$\frac{\partial(\rho' u'_i)}{\partial t'} = -\frac{\partial(\rho' u'_i u'_j)}{\partial x'_j} - \frac{\partial p'_i \delta_{ij}}{\partial x'_j} \frac{p_0}{\rho_0 u_0^2} + \frac{\partial}{\partial x'_j} \left(\mu' \left(\frac{\partial u'_i}{\partial x'_j} + \frac{\partial u'_j}{\partial x'_i} - \frac{2}{3} \frac{\partial u'_k}{\partial x'_k} \delta_{ij} \right) \right) \frac{\mu_0}{\rho_0 u_0 L_0} \tag{1.19}$$

Defining the free-stream Mach number and the Reynolds number as

$$M_\infty = \frac{u_\infty}{\sqrt{\gamma p_0 / \rho_0}} \qquad Re = \frac{\rho_0 u_\infty L_0}{\mu_\infty} \tag{1.20}$$

Equation (1.2) can be recast as

$$\frac{\partial(\rho' u'_i)}{\partial t'} = -\frac{\partial(\rho' u'_i u'_j + p'_i \delta_{ij})}{\partial x'_j} + \frac{\sqrt{\gamma} M_\infty}{Re} \frac{\partial}{\partial x'_j} \left(\mu' \left(\frac{\partial u'_i}{\partial x'_j} + \frac{\partial u'_j}{\partial x'_i} - \frac{2}{3} \frac{\partial u'_k}{\partial x'_k} \delta_{ij} \right) \right) \tag{1.21}$$

Similarly, the energy equation can be transformed as

$$\frac{\partial(\rho' E')}{\partial t'} \frac{\rho_0 u_0}{L_0} \frac{p_0}{\rho_0} = -\frac{\partial}{\partial x'_j}((\rho' E' + p')u'_j)\frac{\rho_0 u_0}{L_0} \frac{p_0}{\rho_0} + \frac{\partial(\sigma_{ij} u_i)}{\partial x_j} + \frac{\partial}{\partial x'_j}\left(\lambda' \frac{\partial T'}{\partial x'_j}\right)\frac{\lambda_0 T_0}{L_0^2} \tag{1.22}$$

where, again,

$$\frac{\partial(\sigma_{ij} u_i)}{\partial x_j} = \frac{\partial}{\partial x'_j}\left(\mu'\left(\frac{\partial u'_i}{\partial x'_j} + \frac{\partial u'_j}{\partial x'_i} - \frac{2}{3}\frac{\partial u'_k}{\partial x'_k}\delta_{ij}\right)u'_i\right)\frac{\mu_0 u_0^2}{L_0^2} \tag{1.23}$$

Dividing Equation (1.22) by $\frac{\rho_0 u_0}{L_0}\frac{p_0}{\rho_0}$ it becomes

$$\frac{\partial(\rho' E')}{\partial t'} = -\frac{\partial}{\partial x'_j}((\rho' E' + p')u'_j) + \frac{\partial}{\partial x'_j}\left(\mu'\left(\frac{\partial u'_i}{\partial x'_j} + \frac{\partial u'_j}{\partial x'_i} - \frac{2}{3}\frac{\partial u'_k}{\partial x'_k}\delta_{ij}\right)u'_i\right)\frac{\mu_0 u_0^2}{L_0^2}\frac{L_0 \rho_0}{\rho_0 u_0 p_0} +$$

$$+ \frac{\partial}{\partial x'_j}\left(\lambda'\frac{\partial T'}{\partial x'_j}\right)\frac{\lambda_0 T_0}{L_0^2}\frac{L_0 \rho_0}{\rho_0 u_0 p_0} \tag{1.24}$$

Knowing that

$$Pr = \frac{\gamma R_0}{\gamma - 1} \frac{\mu_\infty}{\lambda_\infty} \tag{1.25}$$

and remembering the definitions of Mach and Reynolds numbers (1.20), the non-dimensional form of (1.3) is

$$\frac{\partial(\rho' E')}{\partial t'} = -\frac{\partial}{\partial x'_j}((\rho' E' + p')u'_j) +$$

$$+ \frac{\sqrt{\gamma} M_\infty}{Re} \left(\frac{\gamma R_0}{\gamma - 1} \frac{1}{Pr} \frac{\partial}{\partial x'_j} \left(\lambda' \frac{\partial T'}{\partial x'_j} \right) + \frac{\partial}{\partial x'_j} \left(\mu' \left(\frac{\partial u'_i}{\partial x'_j} + \frac{\partial u'_j}{\partial x'_i} - \frac{2}{3} \frac{\partial u'_k}{\partial x'_k} \delta_{ij} \right) u'_i \right) \right) \tag{1.26}$$

Equations (1.16), (1.21) and (1.26) represent the non-dimensional Navier-Stokes equations that were implemented in the code. Since L_0, ρ_0, p_0, T_0 do not appear in the main non-dimensional groups γ, M_∞, Re or Pr, they have all been set to an unitary value; for this reason $R_0 = p_0/(\rho_0 T_0) = 1$ as well. At the same time a definition for the other dimensional groups can be formulated using the non-dimensional ones

$$\gamma = \frac{c_{p0}}{c_{v0}} \qquad u_\infty = \sqrt{\gamma} M_\infty$$

$$\mu_\infty = \frac{\sqrt{\gamma} M_\infty}{Re} \qquad \lambda_\infty = \frac{\gamma}{\gamma - 1} \frac{1}{Pr} \frac{\sqrt{\gamma} M_\infty}{Re} \tag{1.27}$$

Lastly, a non-dimensional form for the closure equations (1.4), (1.8) and (1.9) has to be provided:

$$p' = \rho' T' \tag{1.28}$$

$$E' = \frac{1}{\gamma - 1} \frac{p'}{\rho'} + \frac{1}{2} (u'_i u'_i)^2 \tag{1.29}$$

$$\mu'(T') = T'^{3/2} \left(\frac{1 + S/T_0}{T' + S/T_0} \right) \tag{1.30}$$

In equations (1.16), (1.21) and (1.26) three common entities can be identified:

- A temporal contribution $\frac{\partial \phi}{\partial t}$ due to the temporal variation of physical fields;

- A convective contribution $-\frac{\partial F_j(\phi)}{\partial x_j}$, related to the transport phenomena associated to velocity and pressure fields;

- A diffusive contribution $\frac{\partial F_{vj}(\phi)}{\partial x_j}$ resulting from the thermodynamic behaviour of the gas and the forces exchanged by elementary fluid volumes.

4

2 Turbulent channel

The first approach, historically, to the problem of wall turbulence could not but be experimental; however, the fast-paced advancement in computational power has made numerical studies, especially DNS, more feasible and affordable. The most common configurations implemented to study this phenomenon are the turbulent pipe and the turbulent channel, the two offering universal and concordant statistics. A typical and distinctive feature of wall turbulence is the presence of so called "turbulence streaks" near the wall, as seen in Figure 2.1 below, depicting different cases
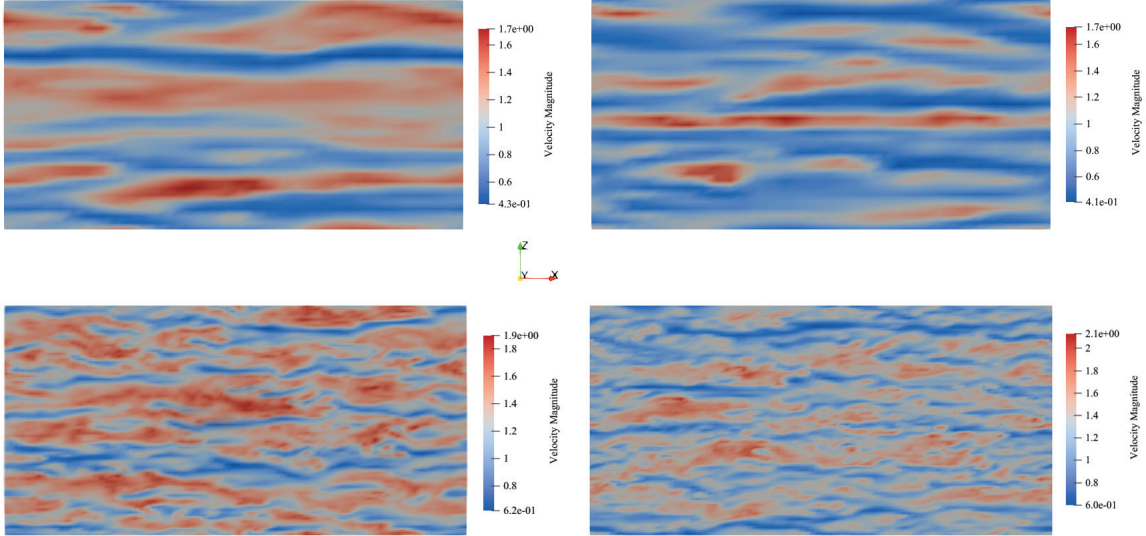

Figure 2.1: Representation of the mean velocity near the bottom wall using a dynamical Smagorinsky (DSMG) model at $Re_\tau = 215$ (top left), $Re_\tau = 500$ (bottom left) and the unresolved approach (ILES) at $Re_\tau = 215$ (top right) and $Re_\tau = 500$ (bottom right).

The expression "turbulent channel" identifies the flow throughout a rectangular duct which is long and has a sufficiently large width-to-height ratio. Most natural and artificial turbulent flows are considered to be bounded, at least in part, to at least one or more solid surfaces. The mean flow is predominantly in the axial direction x while the most relevant mean velocity variations occur especially in the wall-normal direction y. At the same time the flow is statistically independent of z. The wall locations are located at $y = 0, 2h$, so that the channel height is $2h$. Because only the fully developed flow is relevant for the statistics and the first part of the channel, from $x = 0$ to approximately $x = 5h$, is a development region, the boundary condition forces the fluid to recirculate so that the x coordinate can be limited to, say, 2π. The Reynolds number used in association with the channel is

$$Re = \frac{2h\bar{u}}{\nu} \tag{2.1}$$

where $\bar{u}$ is the bulk velocity

$$\bar{u} = \frac{1}{h} \int_0^h \langle u \rangle \, dy \tag{2.2}$$

5

and $\langle u \rangle$ is defined in Equation (3.3). The flow is considered turbulent without observable transitional effects when $Re > 3000$ and in the present study the two examined Reynolds numbers were $Re = 5365$ and $Re = 14386$.

A fully developed channel flow can be defined by the sole variables ρ, $\nu = \frac{\mu}{\rho}$, h and $u_\tau = \sqrt{-\frac{h}{\rho}\frac{dp_w}{dx}} = \sqrt{\frac{\tau_w}{\rho_w}}$, which can form the two non-dimensional groups y/h and $Re_\tau = u_\tau h/\nu$; the mean velocity profile can therefore be written as

$$\langle u \rangle = u_\tau F_0 \left(\frac{y}{h}, Re_\tau \right) \tag{2.3}$$

where F_0 is a non-dimensional function to be determined. However, since the dynamically relevant quantity is $d\langle u \rangle/dy$, and it depends on only two non-dimensional parameters, Equation (2.3) can be restated as

$$\frac{d\langle u \rangle}{dy} = \frac{u_\tau}{y} \Phi \left(\frac{y}{\delta_v}, \frac{y}{h} \right) \tag{2.4}$$

where $\delta_v = \nu_w/u_\tau$ represents the viscous length scale, which will surely be smaller than h, the length scale in the outer layer. After performing the calculations it is clear that $Re_\tau = \left(\frac{y}{\delta_v} \right)/\left(\frac{y}{h} \right)$ so that the two formulations are conceptually related.

In the next two sections, the two fundamental laws that drive the flow — the law-of the wall and the logarithmic law — will be discussed.

2.1 Law-of-the-wall

Ludwig von Prandtl [39] asserted that in the near-wall region ($y/h \ll 1$) the mean velocity profile is governed by the viscous scales alone. In this case then

$$\frac{d\langle u \rangle}{dy} = \frac{u_\tau}{y} \Phi_I \left(\frac{y}{\delta_v} \right) \tag{2.5}$$

where

$$\Phi_I \left(\frac{y}{\delta_v} \right) = \lim_{y/h \to 0} \Phi \left(\frac{y}{\delta_v}, \frac{y}{h} \right) \tag{2.6}$$

In this case $y^+ = y/\delta_v$ is the only quantity that drives the velocity in this part of the channel [41]. The normalised velocity, later used for compressibility transformations and results, is defined as

$$u^+ = \frac{\langle u \rangle}{u_\tau} \tag{2.7}$$

Using these definitions, Equation (2.5) can be rewritten as

$$\frac{du^+}{dy^+} = \frac{1}{y^+} \Phi_I \left(y^+ \right) \tag{2.8}$$

The law of the wall is obtained by integrating Equation (2.8) in y^+:

$$u^+ = F_w(y^+) \tag{2.9}$$

with

$$F_w(y^+) = \int_0^{y^+} \frac{1}{y'} \Phi_I \left(y' \right) dy' \tag{2.10}$$

This result obtained by Prandtl is very meaningful in that it shows a dependency of $u^+ = u/u_\tau$ *solely* on the scaled coordinate y^+, and in particular $u^+ = y^+$. During the years, and in this work as well, the law of the wall has been largely proven valid not only in the region strictly adjacent to the wall, but in the viscous sublayer as well, i.e. $y^+ < 5$.

2.2 Logarithmic law

Moving away from the wall, the importance of viscosity increasingly fades and Φ_I depends more on $\frac{y}{h}$ and less on $\frac{y}{\delta_v}$. Considering again Equation (2.5) Φ_I tends to a constant. Indeed, for $y/h \ll 1$ and $y^+ \gg 1$

$$\Phi_I(t^+) = \frac{1}{\kappa} \tag{2.11}$$

where $\kappa \approx 0.41$ is the von Kármán constant. Therefore, from Equation (2.11)

$$\frac{du^+}{dy^+} = \frac{1}{\kappa y^+} \tag{2.12}$$

By means of integration the mean scaled velocity profile becomes

$$u^+ = \frac{1}{\kappa} \ln y^+ + B \tag{2.13}$$

This logarithmic law of the wall, ideated by von Kármán (1930) [40], works well with the generally agreed upon constants $\kappa = 0.41$ and $B = 0.52$. In Figure 2.2 it is clear how the mean velocity curve follows the linear law of the wall up to $y^+ \simeq 5$ and the logarithmic law from greater values of y^+, roughly $y^+ > 40$. The region in between the two is commonly referred to as the "overlap layer".
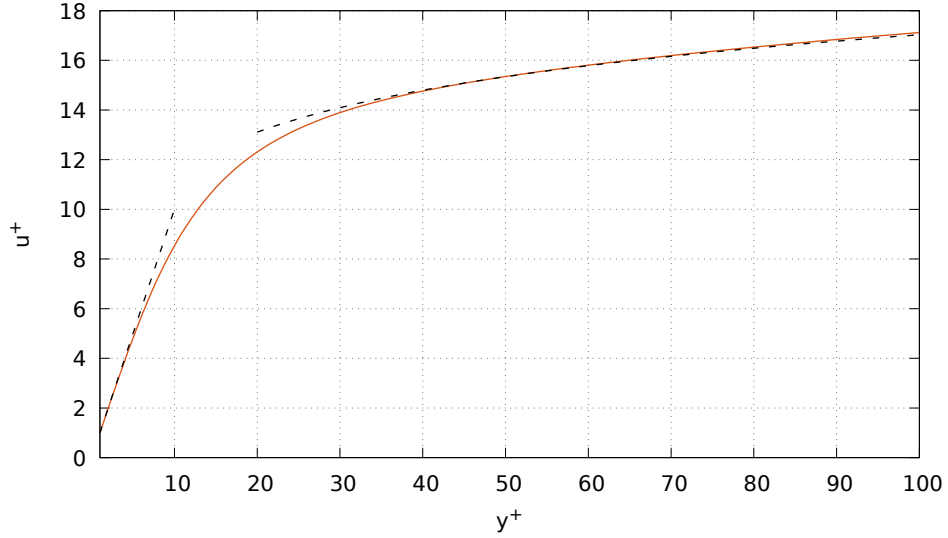
Figure 2.2: Mean velocity curve at $M = 0.1$ and $Re_\tau = 180$ employing the dynamical Smagorinsky (DSMG) model. The dashed lines denote the law-of-the-wall ($y^+ < 10$) and the logarithmic law ($20 < y^+ < 100$).

In the outer layer another law can be considered: given the fact that Φ is practically independent of y/δ_v, it tends asymptotically to a function of y/h, here called Φ_0:

$$\lim_{y/\delta_v \to \infty} \Phi\left(\frac{y}{\delta_v}, \frac{y}{h}\right) = \Phi_0\left(\frac{y}{h}\right) \tag{2.14}$$

Inserting Φ_0 in Equation (2.5) and integrating in y yields

$$\frac{u_0 - \langle u \rangle}{u_\tau} = F_D\left(\frac{y}{h}\right) \tag{2.15}$$

where u_0 is the center-line velocity and

$$F_D\left(\frac{y}{h}\right) = \int_{y/h}^1 \frac{1}{y'} \Phi_0\left(y'\right) dy' \tag{2.16}$$

Equation (2.15) is called the velocity-defect law for obvious reasons. Unlike in the previous laws, F_D is not universal and may depend on the flow and its characteristics. In the buffer layer, as Millikan pointed out, the values provided by the two laws should be overlapping as well.

2.3 Reynolds stresses

In order to coherently study the Reynolds stresses, the flow is better divided into three regions: the viscous wall region, $y^+ < 50$, the log-law region, $50 < y^+ < 120$ and the core, $y^+ > 120$. The scaled

Reynolds stresses are represented as

$$R_{ij} = \tau_{ij} = \frac{u_i'' u_j''}{u_\tau^2} \tag{2.17}$$

where the numerator is obtained using the Favre decomposition, explicited in Equation (3.20), and the denominator scales the stress to make it non-dimensional. In Figure 2.3 a non-logarithmic representation of the Reynolds stresses is shown.
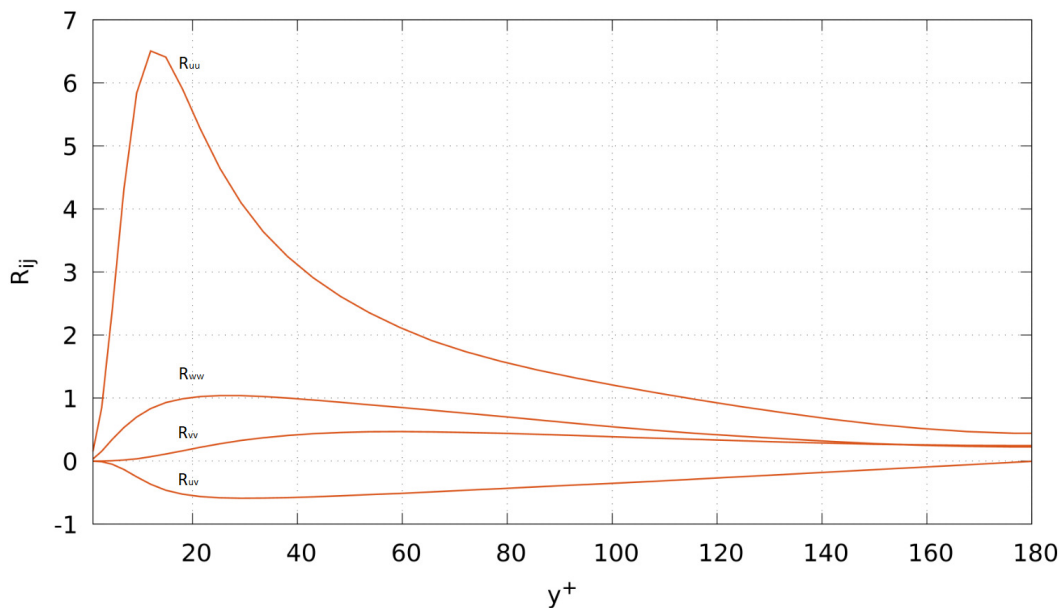

Figure 2.3: Typical Reynolds stresses, obtained at $M = 0.1$ and $Re_\tau = 180$ employing the dynamical Smagorinsky (DSMG) model.

The most intense turbulent activity can be found in the viscous wall region, all the peaks occurring before $y^+ = 60$. In this region, for fixed x, z and t, and for small y, the fluctuating velocity components can be rewritten using Taylor expansions

$$u = a_1 + b_1 y + c_1 y^2 + \dots \tag{2.18}$$

$$v = a_2 + b_2 y + c_2 y^2 + \dots \tag{2.19}$$

$$w = a_3 + b_3 y + c_3 y^2 + \dots \tag{2.20}$$

At the boundary location $y = 0$, the no-slip condition yields $u = a_1 = 0$ and $w = a_3 = 0$, whereas the impermeability one $v = a_3 = 0$; at the same time, from the no-slip condition, $(\partial u/\partial x)_{y=0}$ and $(\partial w/\partial x)_{y=0}$ are zero: the continuity equation then becomes

$$\left(\frac{\partial v}{\partial y}\right)_{y=0} = b_2 = 0 \tag{2.21}$$

9

What this means is that, very close to the wall, the flow just has the u and w components, resulting in a motion parallel to the wall. Keeping in mind the coefficient values, after applying the Favre filtering to Equations (2.18-2.20), multiplying them in the proper way and ignoring higher-order terms, the non-scaled Reynolds stresses can be found:

$$\widetilde{u''u''} \simeq \tilde{b}_1^2 y^2 \tag{2.22}$$

$$\widetilde{v''v''} \simeq \tilde{c}_2^2 y^4 \tag{2.23}$$

$$\widetilde{w''w''} \simeq \tilde{b}_3^2 y^2 \tag{2.24}$$

$$\widetilde{u''v''} \simeq \widetilde{b_1 c_2} y^3 \tag{2.25}$$

The coefficients are not known beforehand but the order of the various y terms is useful to understand how the curves will behave: the R_{uu} and R_{ww} terms increase from zero with y^2, the absolute value of R_{uv} with y^3 and finally R_{vv} is governed by y^4. Since in this region $y < 1$ ($y^+ = 50 \Rightarrow y \simeq 0.29$), the first two components of the tensor will increase the fastest, while the latter will be the slowest. These considerations are confirmed by the trends shown in Figure 2.3.

2.4   Compressible wall turbulence

Possible effects of flow compressibility on the typical length scales associated to wall turbulence have been widely discussed since the introduction of the problem and still are an open issue. For example, while the characteristic length scales seem to not vary with the Reynolds number sufficiently away from the wall, dependence on the Mach number are still unclear. Actually, contrasting or even opposite results have been found for the dimension of characteristic streamwise length scales with respect to increasing Mach numbers. Traditionally, in an incompressible flow the characteristic length scales should increase linearly with the wall distance in the outer layer ($y^+ > 50$) and in particular, according to Mizuno and Jiménez (2011) [37], it should scale with the local mean shear:

$$l_{MJ} \sim u_\tau \left(\frac{d\bar{u}}{dy}\right)^{-1} \tag{2.26}$$

According to Pirozzoli (2012) [38], however, the incompressible length scales should read

$$l_P \sim (u_\tau h) \left(\frac{d\bar{u}}{dy}\right)^{-1/2} \tag{2.27}$$

This formulation has been shown by Pirozzoli himself to be more accurate than the one by Mizuno and Jiménez. This scaling can be easily adapted to the compressible case provided the main compressibility effects are included in the variation of the local friction velocity:

$$l_P^* \sim (u_\tau^* h) \left(\frac{d\tilde{u}}{dy}\right)^{-1/2} \tag{2.28}$$

where $u_\tau^* = u_\tau \sqrt{\rho_w/\rho}$.

3 DNS, RANS & LES

3.1 DNS

Computationally speaking, there are three main approaches to the problem of turbulent channel flows. In a Direct Numerical Simulation (DNS), Equations (1.16), (1.21) and (1.26) are implemented and solved without any turbulence model, meaning every single temporal and spatial scale, from Kolmogorov's microscale to the integral scale, must be resolved in the computational mesh. Needless to say, this method is the most accurate one but it requires the largest amount of time with respect to the other two; both the spatial and the temporal resolutions required by this method exceed the commonly available resources.

3.2 RANS

At the other end of the spectrum are the Reynolds-Averaged Navier-Stokes equations (RANS), a set of averaged equations which again will be directly solved; this method can be implemented using a relatively coarse mesh but it requires "invasive" closure models for the Reynolds stresses and the dissipated energy which can affect the results especially in the boundary layer. Nevertheless, the RANS results are widely known and can represent a useful tool for further understanding the problem of wall turbulence. This approach describes the turbulent flow through its mean behaviour. Let's consider a set of incompressible RANS equations

$$\frac{\partial \langle u_j \rangle}{\partial x_j} = 0 \tag{3.1}$$

$$\frac{\partial \langle u_i \rangle}{\partial t} + \langle u_j \rangle \frac{\partial \langle u_i \rangle}{\partial x_j} = -\frac{1}{\rho}\frac{\partial \langle p \rangle \, \delta_{ij}}{\partial x_j} + \frac{\mu}{\rho}\frac{\partial^2 \langle u_i \rangle}{\partial x_j \partial x_j} - \frac{\partial \langle u_i' u_j' \rangle}{\partial x_j} \tag{3.2}$$

where $\langle \phi \rangle$ represents the Reynolds-average of a flow variable ϕ expressed as

$$\langle \phi \rangle = \lim_{t \to \infty} \frac{1}{\Delta t} \int_{t_0}^{t_0 + \Delta t} \phi\left(t^*\right) dt^* \tag{3.3}$$

and ϕ' its turbulent fluctuation

$$\phi' = \phi - \langle \phi \rangle \tag{3.4}$$

Since the channel presents its interesting features mainly in the wall-normal direction, the x and z dimension are here considered to be much greater, tending to infinity. In this scenario, where also the mean flow is considered stationary and planar ($\langle w \rangle = 0$), both the temporal derivatives and the spatial derivatives along those directions can be neglected:

$$\frac{\partial \langle \phi \rangle}{\partial t} = 0 \tag{3.5}$$

$$\frac{\partial \langle \phi \rangle}{\partial x} = \frac{\partial \langle \phi \rangle}{\partial z} = 0 \tag{3.6}$$

the resulting mass conservation equation

$$\frac{\partial \langle v \rangle}{\partial y} = 0 \tag{3.7}$$

along with the boundary condition for which $\langle v \rangle_{y=0,2h} = 0$ at the wall, makes sure that $\langle v \rangle = 0$ in the whole domain. Knowing this, the momentum conservation equations reduce to

$$-\frac{1}{\rho}\frac{\partial \langle p \rangle}{\partial x} + \frac{\mu}{\rho}\frac{\partial^2 \langle u \rangle}{\partial y^2} - \frac{\partial \langle u'v' \rangle}{\partial y} = 0 \tag{3.8}$$

$$-\frac{1}{\rho}\frac{\partial \langle p \rangle}{\partial y} - \frac{\partial \langle v'^2 \rangle}{\partial y} = 0 \tag{3.9}$$

If the fields in Equation (3.9) do not depend on y, then

$$\langle p \rangle + \rho \langle v'^2 \rangle = f(x) \tag{3.10}$$

which becomes, at the wall location $y = 0$ where $\langle v \rangle = 0$,

$$\langle p \rangle / \rho + \langle v'^2 \rangle = p_w(x)/\rho \tag{3.11}$$

Here $p_w = \langle p(x,0,0) \rangle$ represents the mean pressure on the bottom wall. Computing the derivative of $f(x)$ with respect to x at the wall locations $y = 0, 2h$ yields

$$\frac{df(x)}{dx} = \frac{d}{dx}\left(\langle p \rangle + \rho \langle v'^2 \rangle\right)_{y=0,2h} = \frac{d \langle p \rangle}{dx} = \frac{dp_w}{dx} \tag{3.12}$$

The latter expression indicates that the mean pressure gradient at the wall locations only depends on x. Using this result in Equation (3.8) gives

$$\frac{d \langle p \rangle}{dx} = \frac{\partial}{\partial y}\left(\mu\frac{\partial \langle u \rangle}{\partial y} - \rho \langle u'v' \rangle\right) \tag{3.13}$$

The term in the brackets is dimensionally a shear stress, so

$$\frac{d \langle p \rangle}{dx} = \frac{\partial \tau(y)}{\partial y} \tag{3.14}$$

which means that that the axial normal stress gradient is balanced by the cross-stream shear stress gradient. Equation (3.14) can be integrated to obtain

$$\tau(y) = \frac{d \langle p \rangle}{dx}y + c_1 \tag{3.15}$$

where $c_1 = 0$ due to the symmetry of the domain along y. Because $\tau(y)$ depends solely on y, $\frac{\partial \tau(y)}{\partial y}$ must be constant; since it is also known that $\tau(h) = 0$, it must be $\tau(0) = \tau_w$ and $\tau(2h) = -\tau_w$. Therefore the solution to Equation (3.14) is

$$\frac{\tau_w}{h} = -\frac{dp_w}{dx} \tag{3.16}$$

and

$$\tau(y) = -\frac{d\langle p \rangle}{dx} \frac{|y|}{h} \tag{3.17}$$

It is now clear that the mean pressure gradient is the entity that counterbalances the wall shear stress and ensures the continuous motion of the fluid. In order to correctly simulate the motion of the fluid in the channel, the mean pressure gradient, in the form of an equivalent force or a given friction, must be introduced as a parameter. In this case the former solution has been adopted: the Direct Forcing method keeps the fluid moving while at the same time setting the flow rate value. By expressing the bulk velocity as

$$u_b = \frac{\int_V \rho u dV}{\int_V \rho dV} \tag{3.18}$$

the mean pressure gradient can be written as a function of the deficit between a target speed u_∞ and the actual bulk velocity u_b:

$$\frac{d\langle p \rangle}{dx} = u_\infty - u_b = \mathscr{F} \tag{3.19}$$

The speed deficit $\mathscr{F}$ was in fact used as a forcing term in the Navier-Stokes equations. Thus, the periodic boundary conditions of Section 5.4 could be implemented.

3.3 LES

In this instance various versions of a Large Eddy Simulation (LES) have been used. Proposed in 1963 by American meteorologist Joseph Smagorinsky [6] to simulate atmospheric air currents, it relies on the famous Kolmogorov's hypothesis (1941) [7] to obtain accurate results with less of a computational burden. Kolmogorov ingeniously observed that in a turbulent flow, macroscopically, there is an evident directionality but, zooming in, the vortices become substantially isotropic and homogeneous: small scale vortices are therefore statistically universal and are not influenced by the geometry of the channel nor any bodies immersed in the fluid. This approach simulates the bigger vortices as a DNS would do but it requires the implementation of a model for the smaller scales that accounts for the viscous dissipation as well. In order to implement the LES equations, a filtering operator is introduced. Since the physical velocity of the fluid consists of different frequencies inversely proportional to the length scales of the vortices, a low pass filter will eliminate the higher frequency "signals" and preserve the ones generated by the bigger vortical structures. Favre filtering of a generic flow variable ϕ is defined as

$$\phi = \tilde{\phi} + \phi'' \tag{3.20}$$

with

$$\tilde{\phi} = \frac{\overline{\rho\phi}}{\bar{\rho}} \tag{3.21}$$

Here $\overline{(\cdot)}$ is the generic spatially filtered variable. Applying the operator, the non-dimensional Navier-Stokes equations (1.16), (1.21), (1.26) become

$$\frac{\partial \bar{\rho}}{\partial t} = -\frac{\partial(\bar{\rho}\tilde{u}_i)}{\partial x_i} \tag{3.22}$$

13

$$\frac{\partial(\bar{\rho}\tilde{u}_i)}{\partial t} = -\frac{\partial(\bar{\rho}\tilde{u}_i\tilde{u}_j + \bar{p}_i\delta_{ij})}{\partial x_j} + \frac{\sqrt{\gamma}M_\infty}{Re}\frac{\partial}{\partial x_j}\left(\bar{\mu}\bar{d}_{ij}\right)$$

$$-\frac{\partial}{\partial x_j}\left(\overline{\rho u_i u_j} - \bar{\rho}\tilde{u}_i\tilde{u}_j\right) \quad (3.23)$$

$$\frac{\partial(\bar{\rho}\tilde{E})}{\partial t'} = -\frac{\partial}{\partial x_j}((\bar{\rho}\tilde{E} + \tilde{p})\tilde{u}_j) +$$

$$+ \frac{\sqrt{\gamma}M_\infty}{Re}\left(\frac{\gamma}{\gamma-1}\frac{1}{Pr}\frac{\partial}{\partial x_j}\left(\lambda\frac{\partial\tilde{T}}{\partial x_j}\right) + \frac{\partial}{\partial x_j}\left(\bar{\mu}\bar{d}_{ij}\tilde{u}_i\right)\right)$$

$$-\frac{\partial}{\partial x_j}\left(\overline{(\rho E + p)\,u_i} - (\bar{\rho}\tilde{E} + \bar{p})\tilde{u}_i\right) \quad (3.24)$$

where the stress tensor is defined by

$$\bar{d}_{ij} = \left(\frac{\partial\tilde{u}_i}{\partial x_j} + \frac{\partial\tilde{u}_j}{\partial x_i} - \frac{2}{3}\frac{\partial\tilde{u}_k}{\partial x_k}\delta_{ij}\right) \quad (3.25)$$

It can be noted that while the first equation, once again, remains formally identical to itself, Equations (3.23) and (3.24) present additional contributions linked to the subgrid-scale stress tensor and subgrid-scale energy terms respectively; both these newly found entities introduce yet another closure problem, which has been addressed in different ways, all implemented in the Unsteady Robust All-around Navier-StOkes Solver (URANOS) and presented in this work. Comparing Equations (3.23), (3.24) to their non-filtered counterparts, new terms concerning the divergence of subgrid-scale stress tensor and energy, respectively, appear. These new contributions, expressed by

$$\overline{T}_{ij}^{SGS} = \overline{\rho u_i u_j} - \bar{\rho}\tilde{u}_i\tilde{u}_j \quad (3.26)$$

$$\overline{E}_j^{SGS} = \overline{(\rho E + p)\,u_i} - (\bar{\rho}\tilde{E} + \bar{p})\tilde{u}_i = \overline{\rho c_p T u_j} - \bar{\rho}\bar{c}_p\tilde{T}\tilde{u}_j + \frac{1}{2}\overline{T}_{ij}^{SGS}\tilde{u}_j - \frac{1}{2}\overline{T}_{kk}^{SGS}\tilde{u}_j \quad (3.27)$$

represent the contributions that, due to the filtering process, are not resolved. The hardest challenge in the LES approach is to find a suitable model to account for these subgrid phenomena. According to Boussinesq's hypothesis regarding Reynolds stresses and mean strain [7], the non-spherical components of the stress tensor can be expressed as

$$\overline{T}_{ij}^{SGS} - \frac{1}{3}\overline{T}_{kk}^{SGS}\delta_{ij} = -2\mu_{SGS}\left(\widetilde{S}_{ij} - \frac{1}{3}\widetilde{S}_{kk}\delta_{ij}\right) \quad (3.28)$$

where μ_{SGS} is the subgrid turbulent eddy viscosity, the main parameter that will be modelled by the various methods, and $\widetilde{S}_{ij}$ represents the resolved strain-rate tensor

$$\widetilde{S}_{ij} = \frac{1}{2}\left(\frac{\partial\tilde{u}_i}{\partial x_j} + \frac{\partial\tilde{u}_j}{\partial x_i}\right) \quad (3.29)$$

The last version of Equation (3.27) for the energy subgrid-scale components can be modelled in similar fashion:

$$\overline{E}_j^{SGS} = -\lambda_{SGS}\frac{\partial\tilde{T}}{\partial x_j} + \frac{1}{2}\overline{T}_{ij}^{SGS}\tilde{u}_j - \frac{1}{2}\overline{T}_{kk}^{SGS}\tilde{u}_j \quad (3.30)$$

14

where λ_{SGS} is the subgrid-scale turbulent diffusivity

$$\lambda_{SGS} = \mu_{SGS}\frac{\bar{c}_p}{Pr_T} \tag{3.31}$$

and $Pr_T = 0.9$. Using those previous assumption and discarding the isotropic contribution $\overline{T}_{kk}^{SGS}$ [11, 12], the filtered Navier-Stokes that will be used in the LES are

$$\frac{\partial\bar{\rho}}{\partial t} = -\frac{\partial(\bar{\rho}\tilde{u}_i)}{\partial x_i} \tag{3.32}$$

$$\frac{\partial(\bar{\rho}\tilde{u}_i)}{\partial t} = -\frac{\partial}{\partial x_j}(\bar{\rho}\tilde{u}_i\tilde{u}_j + \bar{p}_i\delta_{ij}) + \frac{\sqrt{\gamma}M_\infty}{Re}\frac{\partial}{\partial x_j}\left(\bar{\mu}_{tot}\bar{d}_{ij}\right) \tag{3.33}$$

$$\frac{\partial(\bar{\rho}\tilde{E})}{\partial t'} = -\frac{\partial}{\partial x_j}((\bar{\rho}\tilde{E} + \tilde{p})\tilde{u}_j) + \frac{\sqrt{\gamma}M_\infty}{Re}\left(\bar{\lambda}_{tot}\frac{\partial}{\partial x_j}\left(\lambda\frac{\partial\tilde{T}}{\partial x_j}\right) + \frac{\partial}{\partial x_j}\left(\bar{\mu}\bar{d}_{ij}\tilde{u}_i\right)\right) \tag{3.34}$$

where

$$\bar{\mu}_{tot} = \mu(\tilde{T}) + \frac{Re}{\sqrt{\gamma}M}\mu_{SGS} \tag{3.35}$$

and

$$\bar{\lambda}_{tot} = \frac{\gamma}{\gamma - 1}\left(\frac{\mu(\tilde{T})}{Pr} + \frac{Re}{\sqrt{\gamma}M}\frac{\mu_{SGS}}{Pr_T}\right) \tag{3.36}$$

are the total dynamic viscosity (molecular and subgrid-scale) and the total diffusivity of the flow respectively. The most important issue about the LES approach is to find an efficient modelisation of the new unknown μ_{SGS} at the Kolmogorov scale. The generic model employed today employs algebraic — not differential — equations in which different entities come into play, as can be seen in Equation (3.37)

$$\mu_{SGS} = \bar{\rho}(C_m\Delta)^2\mathcal{D}_m\left[\bar{\mathbf{U}}\right] \tag{3.37}$$

where C_m is a tuning parameter, different for every model, $\Delta = V^{1/3} = (\Delta_x\Delta_y\Delta_z)^{1/3}$ is the subgrid characteristic length and $\mathcal{D}_m\left[\bar{\mathbf{U}}\right]$ is the non-linear differential operator applied to the resolved flow quantities $\bar{\mathbf{U}}$. Along with a non-resolved formulation for Equations (3.32, 3.33, 3.34), which will be called "ILES" or "unresolved LES", three different models have been taken into account: the Smagorinsky dynamic model (DSMG), the Wall-Adapted Large-Eddy viscosity model (WALE), the Sigma model (SGMA) and the Mixed Time Scale model (MXTS).

3.3.1 Smagorinsky model

The Smagorinsky model is based on the assumption of the balance between the energy production and dissipation effects in the equation for subgrid-scale kinetic energy. This modelisation is the simplest when it comes to evaluate μ_{SGS}. In this case the differential operator is defined as (see also Equation (3.29))

$$\mathcal{D}_m\left[\bar{\mathbf{U}}\right] = \sqrt{2\tilde{S}_{ij}\tilde{S}_{ij}} \tag{3.38}$$

In the *classic* Smagorinsky model the coefficient C is fixed to

$$C_s = \frac{1}{\pi} \left(\frac{3K_0}{2} \right)^{-3/4} \simeq 0.18 \tag{3.39}$$

(with $K_0 = 1.4$), which was found to cause excessive damping of large scale fluctuations. For this reason Germano et al. (1991) [49] proposed to dynamically compute its value at every step based on a space and time dependent relationship. Figure 3.1-3.4 show the trends of $\mu_{SGS}/\bar{\mu}$ up to the channel's center line with the different approaches at $M = 1.5$ and $Re_\tau = 500$.
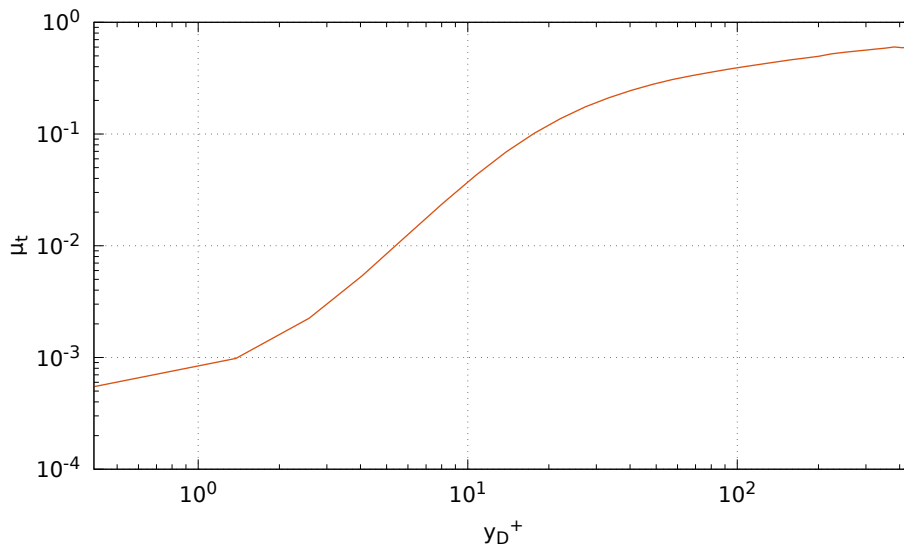

Figure 3.1: $\mu_{SGS}/\bar{\mu}$ profile using a dynamical Smagorinsky (DSMG) model at $M = 1.5$ and $Re_\tau = 500$.

3.3.2 Wall-Adaptive Large-Eddy model

This formulation was introduced in 1999 by Nicoud and Ducros (1999) [12] and its purpose is to resolve μ_{SGS} especially accurately in the near-wall region. In this particular model $\mathcal{D}_m \left[\bar{\mathbf{U}} \right]$ is defined as

$$\mathcal{D}_m \left[\bar{\mathbf{U}} \right] = \frac{\left(S_{ij}^d S_{ij}^d \right)^{3/2}}{\left(S_{ij} S_{ij} \right)^{5/2} + \left(S_{ij}^d S_{ij}^d \right)^{5/4}} \tag{3.40}$$

where

$$S_{ij}^d = \frac{1}{2} \left(\frac{\partial \tilde{u}_i}{\partial x_l} \frac{\partial \tilde{u}_l}{\partial x_j} + \frac{\partial \tilde{u}_j}{\partial x_l} \frac{\partial \tilde{u}_l}{\partial x_i} \right) - \frac{1}{3} \frac{\partial \tilde{u}_m}{\partial x_l} \frac{\partial \tilde{u}_l}{\partial x_m} \delta_{ij} \tag{3.41}$$

is the traceless symmetric part of the square of the resolved velocity gradient tensor. The tuning parameter is given by $C_w = \sqrt{10.6 C_s}$.

16

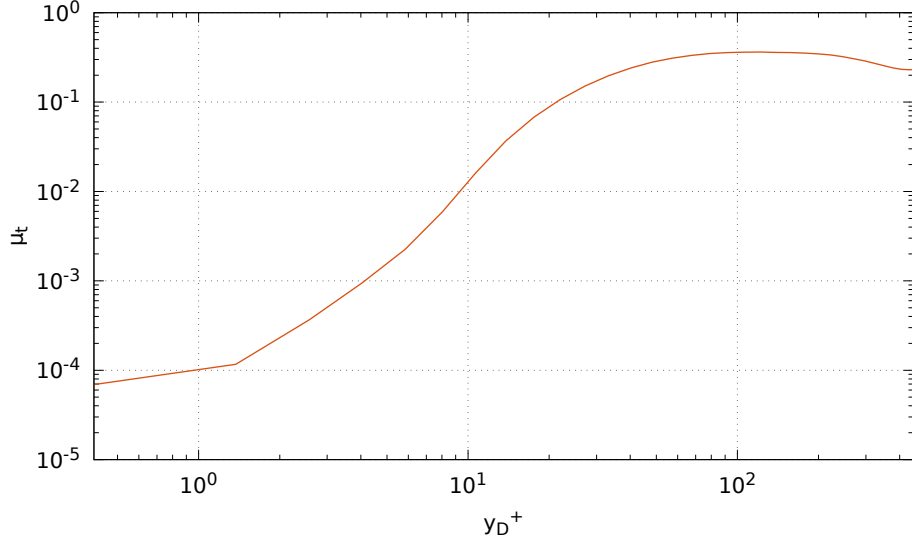Figure 3.2: $\mu_{SGS}/\bar{\mu}$ profile using a wall-adaptive large-eddy (WALE) model at $M = 1.5$ and $Re_\tau = 500$.

3.3.3   SIGMA model

This model, formulated by Kuhn (1986) [13] aims at fulfilling three properties of the fluid:

- $\mathcal{D}_m\left[\bar{\mathbf{U}}\right]$ should be asymptotically less relevant while nearing the wall;

- μ_{SGS} should be zero in the case of a solid rotating flow and of pure shear;

- μ_{SGS} should be zero in the case of axisymmetric or isotropic contraction/expansion at the subgrid level.

For these reasons, given the tensor

$$G_{ij} = \frac{\partial \tilde{u}_i}{\partial x_j} \frac{\partial \tilde{u}_j}{\partial x_i} \tag{3.42}$$

the differential operator $\mathcal{D}_m\left[\bar{\mathbf{U}}\right]$ has been defined as

$$\mathcal{D}_m\left[\bar{\mathbf{U}}\right] = \frac{\sigma_3\left(\sigma_1 - \sigma_2\right)\left(\sigma_2 - \sigma_3\right)}{\sigma_1^2} \tag{3.43}$$

where $\sigma_1 > \sigma_2 > \sigma_3 \geq 0$ are the square roots of the eigenvalues of the G_{ij} tensor, which represent the singular values of the velocity gradient.
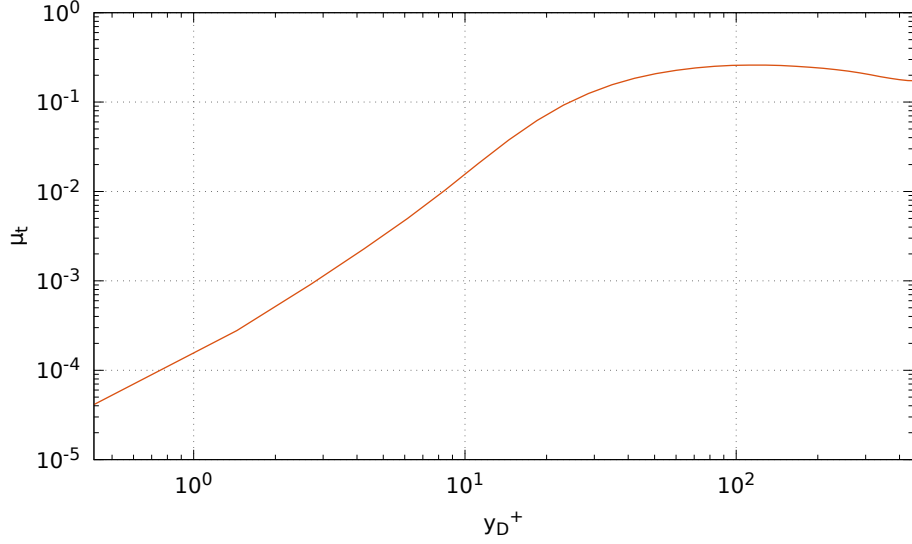
Figure 3.3: $\mu_{SGS}/\bar{\mu}$ profile using a sigma (SGMA) model at $M = 1.5$ and $Re_\tau = 500$.

Confronting the four methods, the most noticeable difference is clearly the viscosity trend in the Smagorinsky model, where monotonically increases until the channel mid-line. The other methods reflect the typical course of the viscosity curve in a turbulent channel flow [14].

3.3.4   Mixed Time Scale model

Developed by Inagaki et al. (2005) [15], this model aims to avoid the use of a model parameter that has to be adjusted according to the type of flow field, and to eliminate the subgrid-scale effect in the laminar flow region. In order to do so, Inagaki considered the Smagorinsky expression

$$\mu_{SGS} = \bar{\rho}(fC_s\Delta)^2 \mathcal{D}_m\left[\bar{\mathbf{U}}\right] = fC_\nu \Delta \sqrt{k} \tag{3.44}$$

where $\mathcal{D}_m\left[\bar{\mathbf{U}}\right]$ obeys to the Smagorinsky model (3.38) and f is a wall-damping function. $\sqrt{k}$ represents the velocity scale as k is the subgrid-scale turbulent energy, which can be estimated by

$$k_{es} = (\bar{u_k} - \widehat{\widetilde{u_k}})^2 \tag{3.45}$$

where $\widehat{\widetilde{u_k}}$ represents a velocity filtered adopting the Simpson rule. Inagaki's idea was to consider $1/\mathcal{D}_m\left[\bar{\mathbf{U}}\right]$ as the time scale so that $\mu_{SGS} \propto \bar{\rho} * k/\mathcal{D}_m\left[\bar{\mathbf{U}}\right]$, i.e. $\mu_{SGS} \propto \bar{\rho} * (Velocity\ scale)^2 * (Time\ scale)$; by doing this, there is no need for a damping function f. This method has been shown to agree well with other subgrid-scale models incorporated with a van Driest-type damping function. The complete formulation of the model is

$$\mu_{SGS} = \bar{\rho}C_{MTS}k_{es}T_S, \tag{3.46}$$

$$T_S^{-1} = \left(\frac{\Delta}{\sqrt{k_{es}}} \right)^{-1} + \left(\frac{C_T}{\mathcal{D}_m \left[\bar{\mathbf{U}} \right]} \right)^{-1} \qquad (3.47)$$

The model parameters C_{MTS} and C_T are fixed to 0.05 and 10 respectively, according to Inagaki's results. As can be easily seen, the time scale is defined as the harmonic average of $\Delta/\sqrt{k_{es}}$, corresponding to the small-scale turbulence, and $1/\mathcal{D}_m[\bar{\mathbf{U}}]$, relative to the larger scales. The time scale in this model approaches the latter formulation nearing the wall so that a wall-damping function is not required.
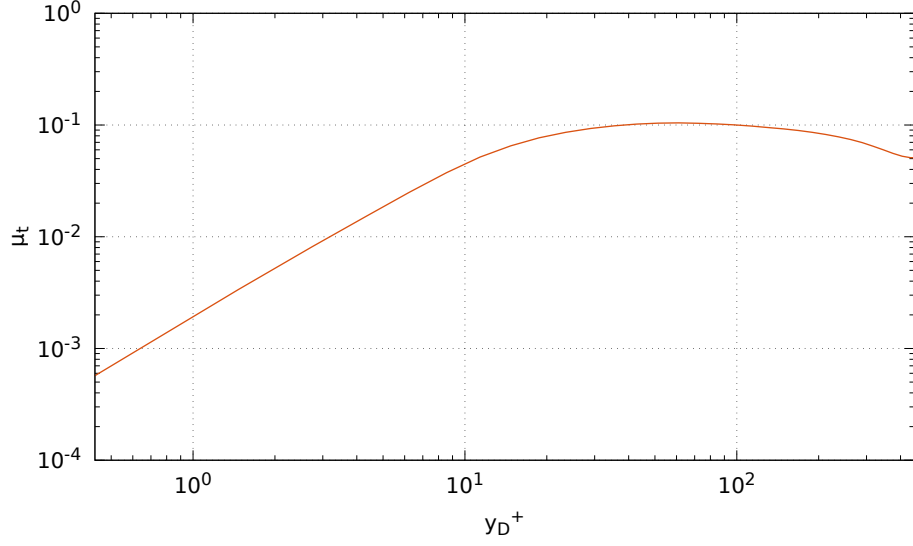

Figure 3.4: $\mu_{SGS}/\bar{\mu}$ profile using a mixed time scale (MXTS) model at $M = 1.5$ and $Re_\tau = 500$.

4   Compressibility transformations

In the compressible flows studied in this work, compressibility effects are relevant, especially at the high Mach number used. In order to be able to compare the results and have a common system of reference, besides making the equations non-dimensional and averaged, different types of compressibility transformations were implemented and applied to the results. This procedure turns the compressible results into incompressible ones, which have already been fully investigated with a DNS approach. Over the years, a number of different transformations have been proposed, one of the first being the Howarth-Dorodnitsyn transformation (1942), used in laminar boundary layer flows. As will be seen later on, the Morkovin hypothesis (1962) [39] for boundary layers still holds: in his work, the Czech engineer postulated that in non-hypersonic boundary layers compressibility effects are negligible so the mean flow profiles are expected to collapse to the corresponding incompressible distributions with variations only in mean density and viscosity. Besides the velocity profiles, all the proposed transformation also rescale the wall-normal coordinate, thus reducing the transformed boundary layer equations to the incompressible ones. This method is powerful because of the basic universality of the inner layer profiles when expressed in a local scaling. However, in turbulent wall layers, no analytical transformation can be found to rigorously transform the governing equations to the incompressible ones; the only provable result is only valid for the viscous sublayer, i.e. $y^+ < 5$, whose relations are shown in Table 1. This is due to the fact that viscous heating in compressible flows causes non-uniform mean density and viscosity, which results in a mean velocity profile that no longer satisfies the law-of-the-wall. What different studies tried, and partially succeeded, to achieve was to generalise the already existing transformations in order to obtain an "incompressible" mean velocity profile that would satisfy the law-of-the-wall in the inner layer.

Using a brilliant generalisation method by Modesti and Pirozzoli (2016) [17] all the relevant transformations, i.e. those by van Driest (1951) [18], Huang et al. (1995) [19], Brun et al. (2008) [20] and most importantly Trettel and Larsson (2014) [21] can be identified. These transformations for both the wall-normal direction and the mean velocity are described by

$$y_I = \int_0^y f_I dy \qquad u_I = \int_0^{\tilde{u}} g_I d\tilde{u} \tag{4.1}$$

where the generic subscript I indicates the different type of transformation, defined in Table 1:

Table 4.1: Mapping functions for wall distance, mean velocity and Reynolds stresses to be used in the generalised transformation relations expressed in Equation (4.1).

Transformation	Wall distance f_I	Mean velocity g_I	Stresses φ_I
Viscous sublayer	$f_V = 1$	$g_V = RN$	NA
Van Driest	$f_D = 1$	$g_D = R^{1/2}$	$\varphi_D = R$
Huang et al.	$f_H = \frac{d}{dy}\left(\frac{y}{R^{1/2}N}\right)$	$g_H = R^{1/2}\left(1 + \frac{\tilde{u}}{R}\frac{dR}{dy}\frac{dy}{d\tilde{u}}\right)$	$\varphi_H = R$
Brun et al.	$f_B = \frac{1}{RN}$	$g_B = \frac{y}{R^{1/2}N}\frac{y}{y_B}$	$\varphi_B = \frac{1}{RN^2}\left(\frac{y}{y_B}\right)^2$
Trettel and Larsson	$f_T = \frac{d}{dy}\left(\frac{y}{R^{1/2}N}\right)$	$g_T = RN\frac{d}{dy}\left(\frac{y}{R^{1/2}N}\right)$	$\varphi_T = R$

where $R = \bar{\rho}/\bar{\rho}_w$ and $N = \bar{\nu}/\bar{\nu}_w$. In their work, Modesti and Pirozzoli found a general rule or constraint which defines a class of compressibility transformations that satisfy the universality of turbulent stresses, expressed in Equation (4.4). The result they found is

$$\frac{\bar{\mu}}{\mu_w}\frac{f_I}{g_I} = 1 \tag{4.2}$$

In this work the traditionally meaningful van Driest transformation and the more recent and accurate Trettel and Larsson transformation were taken into account, for the reasons specified in the next Sections.

4.1   Van Driest transformation

Since its introduction in the early 1950s, the van Driest transformation has been part of the commonly adopted paradigm because of its well established accuracy in inner layers over adiabatic walls ([17], [22]). As said before, assessment of the effectiveness of this transformation is easy thanks to the existence of a "law-of-the-wall" formulated by Prandtl and von Kármán ([39], [40], [23]) for incompressible flows:

$$\frac{u}{u_\tau} = f\left(\frac{y\rho u_\tau}{\mu}\right) \tag{4.3}$$

where f is a certain function and $u_\tau = \sqrt{\tau_w/\rho_w}$ the friction velocity. While the viscous sublayer formulation still holds in the inner region, it loses accuracy towards the outer layer, again, because of viscous heating. Van Driest's idea was to ensure the mean momentum balance in the turbulent channel flow

$$\bar{\mu}\frac{d\tilde{u}}{dy} - \bar{\rho}\widetilde{u''v''} = \bar{\rho}_w u_\tau^2\left(1-\eta\right) = \tau_w\left(1-\eta\right) \tag{4.4}$$

where $\eta = y/h$ is the outer-scaled wall-normal coordinate. Assuming to be sufficiently away from the wall, molecular viscosity becomes negligible; if, at the same time, $\eta \ll 1$, Equation (4.4) becomes

$$-\widetilde{u''v''} \approx \left(\frac{\bar{\rho}_w}{\bar{\rho}}\right)u_\tau^2 = \frac{\tau_w}{\bar{\rho}} \tag{4.5}$$

which shows that the "compressible" stresses, scaled by the local mean density, yield the incompressible behaviour.

Van Driest's transformation relies on the assumption that the main effect of compressibility is a mere mean property variation: the scaled velocity $u^+ = u/u_\tau$ becomes, as pointed out in Table 1

$$u_D^+ = \int_0^{u^+}\left(\frac{\bar{\rho}}{\rho_w}\right)^{1/2}du^+ \tag{4.6}$$

This velocity is used in combination with the transformed coordinate $y_D^+ = y\rho_w\sqrt{\tau_w/\rho_w}/\mu_w$ to recompose the original law-of-the-wall in the form of $u_D^+ = y_D^+$.

The transformation's accuracy for flows over adiabatic walls has been well established during the years in both experiments and DNS up to hypersonic velocities but it does not perform as well in the present case, where the whirling fluid generates heat because of the friction with itself while passing through the channel, especially at higher Mach numbers. Since the boundary conditions force the

exiting fluid to re-enter the channel in order to sustain the turbulent flow, there is the need to dispose of excess heat to maintain the nominal flow conditions. Thus adiabatic walls are replaced by cooled, isothermal ones, with a negative heat transfer rate q_w. The accuracy of the van Driest transformation deteriorates for increasingly negative q_w (see [22]).

4.2 Trettel and Larsson transformation

For the reasons explained above, Trettel and Larsson (see [21]) implemented a new velocity transformation which would satisfy the law-of-the-wall regardless of Reynolds and Mach numbers and q_w. Their transformation focuses on finding a viable log-law condition and a valid stress balance condition. What the "raw" compressible state and the transformed incompressible one have in common are the values at the wall: ρ_w, μ_w and τ_w. This ensures that the friction velocity $u_\tau = (\tau_w/\rho_w)^{1/2}$, the viscous length scale $l_v = \mu_w/(\rho_w u_\tau)$ and the Reynolds stress scale u_τ^2 are the same. While in the van Driest transformation it was implicitly assumed that the transformed coordinate was the same as the original one, Huang et al. (1995) [19] proposed a new coordinate transformation, later adopted by Trettel and Larsson too. This transformation adopts a differential approach: the complete procedure to obtain the transformed variables is given by

$$\frac{dU}{dY} = \frac{dU}{du}\frac{du}{dy}\frac{dy}{dY} \tag{4.7}$$

where U, Y represent the transformed, incompressible variables and u, y the "raw", compressible ones.

4.2.1 Log-law condition

According to Bradshaw [24], since in the log-layer viscous effects are unimportant, the relevant variables are τ_w, $\bar{\rho}$ and y; the velocity scale is therefore $\sqrt{\tau_w/\bar{\rho}}$, while the length scale is y itself. Employing a velocity gradient form,

$$\frac{du}{dy} = \frac{1}{\kappa}\frac{1}{y}\left(\frac{\tau_w}{\bar{\rho}}\right)^{1/2} \qquad \frac{dU}{dY} = \frac{1}{\kappa}\frac{1}{Y}\left(\frac{\tau_w}{\rho_w}\right)^{1/2} \tag{4.8}$$

with $\kappa = 0.436$. Upon rearrangement,

$$\frac{dU}{dY} = \frac{y}{Y}\left(\frac{\bar{\rho}}{\rho_w}\right)^{1/2}\frac{du}{dy} \tag{4.9}$$

While the implicit hypothesis of van Driest was $Y = y$, in this case Trettel and Larsson sought to apply another constraint in order to account for the coordinate transformation as well.

4.2.2 Stress balance condition

The van Driest transformation adjusts the velocity gradients shown in Equation (4.7) in order to obtain the correct slope of the curve; however, that approach does not aim to fulfill the momentum conservation, which Trettel and Larsson found important to do, for the velocity gradients determine the viscous stresses. Generally speaking, the stress balance equation in the inner layer is defined by

$$\bar{\mu}\frac{d\bar{u}}{dy} - \bar{\rho}\widetilde{u'v'} = \tau_{total}(y) \approx \tau_w \tag{4.10}$$

22

where the first addendum represents the viscous stresses and the second one the Reynolds stresses. Since the value of τ_w is the same in both the compressible and incompressible states and $\widetilde{u'v'}$ represents a Reynolds stress, the two scenarios can be compared as follows:

$$\mu_w \frac{dU}{dY} - \rho_w R_{uv} = \bar{\mu} \frac{du}{dy} - \bar{\rho} r_{uv} \approx \tau_w \tag{4.11}$$

According to Morkovin's hypothesis, "the essential dynamics of supersonic boundary layer shear flows will follow the incompressible pattern" [25] so that the viscous addendum in both terms is negligible. After non-dimensionalising using u_τ^2 and rearranging, the so called Morkovin's scaling appears:

$$R_{uv}^+ = \frac{\bar{\rho} r_{uv}}{\tau_w} \tag{4.12}$$

The next step in Trettel and Larsson's reasoning is that this scaling can be applied not only in the boundary layer but in every region of the channel. So, if $\rho_w R_{uv} = \bar{\rho} r_{uv}$, from Equation (4.12) it can be easily concluded that

$$\mu_w \frac{dU}{dY} = \bar{\mu} \frac{du}{dy} \tag{4.13}$$

which means that, if the extension of Morkovin's hypothesis is correct, a balance in the Reynolds stresses implies a balance in the viscous stresses as well. From Equation (4.12) directly follows that

$$\frac{dU}{dY} = \frac{\bar{\mu}}{\mu_w} \frac{du}{dy} \tag{4.14}$$

and

$$\frac{dU}{du} = \left(\frac{\bar{\mu}}{\mu_w} \right) \frac{dY}{dy} \tag{4.15}$$

which collapses to the viscous sublayer transformation (see Table 1) in the case of $dY/dy = 1$; the only difference is that in the viscous sublayer case, Reynolds shear stresses were assumed to be zero, while here they are assumed to be the same in the compressible and incompressible states.

4.2.3 Complete transformation

In conclusion, equalling Equations (4.8) and (4.13) yields

$$\frac{y}{Y} \left(\frac{\bar{\rho}}{\rho_w} \right)^{1/2} \frac{du}{dy} = \frac{\bar{\mu}}{\mu_w} \frac{du}{dy} \tag{4.16}$$

from which can be obtained

$$Y = \left(\frac{\mu_w}{\bar{\mu}} \right) \left(\frac{\bar{\rho}}{\rho_w} \right)^{1/2} y \tag{4.17}$$

The dimensionless form, and the one that has been used in this work, is therefore

$$Y_T^+ = \frac{(\tau_w \bar{\rho})^{1/2}}{\bar{\mu}} y \tag{4.18}$$

Having derived Trettel and Larsson's transformation for the y coordinate, the velocity transformation can be found by differentiating Equation (4.16) and substituting the expression for ${}^{dY}/_{dy}$ into Equation (4.14):

$$\frac{dY}{dy} = \frac{\mu_w}{\bar{\mu}} \left(\frac{\bar{\rho}}{\rho_w}\right)^{1/2} \left[1 + \frac{1}{2}\frac{1}{\bar{\rho}}\frac{d\bar{\rho}}{dy}y - \frac{1}{\bar{\mu}}\frac{d\bar{\mu}}{dy}y\right] \tag{4.19}$$

$$\frac{dU}{du} = \left(\frac{\bar{\rho}}{\rho_w}\right)^{1/2} \left[1 + \frac{1}{2}\frac{1}{\bar{\rho}}\frac{d\bar{\rho}}{dy}y - \frac{1}{\bar{\mu}}\frac{d\bar{\mu}}{dy}y\right] \tag{4.20}$$

The complete velocity transformation can be found by integrating Equation (4.19) using the dimensionless compressible velocity u^+:

$$U_T^+ = \int_0^{u^+} \left(\frac{\bar{\rho}}{\rho_w}\right)^{1/2} \left[1 + \frac{1}{2}\frac{1}{\bar{\rho}}\frac{d\bar{\rho}}{dy}y - \frac{1}{\bar{\mu}}\frac{d\bar{\mu}}{dy}y\right] du^+ \tag{4.21}$$

The transformed Reynolds stresses are expressed in Equation (4.11) while the transformed friction Reynolds number for the channel is

$$Re_\tau^* = \frac{\rho_{c(\tau_w/\rho_c)^{1/2}h}}{\mu_c} \tag{4.22}$$

where h is the channel's half-height.

The weakness of this transformation is that it does not provide a better result for the Reynolds stresses with respect to the van Driest transformation; in fact, the two are the same. For this reason, the Reynolds stresses presented in this work, which follow the van Driest transformation, are not as accurate as the velocity profiles.

5 Solver model

5.1 URANOS

Any ordinary differential equation can be written in the form

$$\begin{cases} y'\,(t) = f\,(t, y\,(t)) & t > t_0 \\ y\,(t_0) = y_0 \end{cases} \tag{5.1}$$

$y : \mathbb{R} \to \mathbb{R}$ being a real function where $y\,(t) \in C^1\,(\mathbb{R})$. This is also the case of the Navier-Stokes equations: $f\,(\cdot)$ becomes the non-linear differential operator $\mathcal{N}\,[\cdot]$ and the non-dimensional equations

$$\frac{\partial \mathbf{U}}{\partial t} = -\frac{\partial \mathbf{F}_j(\mathbf{U})}{\partial x_j} + \frac{\partial \mathbf{F}_{vj}(\mathbf{U})}{\partial x_j} \tag{5.2}$$

become

$$\frac{d\mathbf{U}\,(t)}{dt} = \mathcal{N}\,[t, \mathbf{U}] \tag{5.3}$$

The numerical methods employed to solve this kind of differential equation can be grossly divided into two categories: the *one-stage* methods and the *multi-stage* methods.

In a one-stage method, the more straightforward one, the solution $\mathbf{U}_{n+1}$ at the time step t_{n+1} is obtained from the solution $\mathbf{U}_n$ at the previous time step t_n. This can be done by discretising the originally continuous time axis with

$$t = t_0 + n\Delta t \qquad n \in \mathbb{N} \tag{5.4}$$

and seeking an approximate solution $\mathbf{U}_n$ employing different methods, the more utilised being the Euler, Crank-Nicolson and Runge-Kutta ones; $\mathbf{U}_{n+1}$ can then be found by means of an explicit or implicit formulations, the two being respectively

$$\mathbf{U}_{n+1} = \mathbf{U}_n + \Delta t \mathcal{N}\,[t_n, \mathbf{U}_n] \tag{5.5}$$

$$\mathbf{U}_{n+1} = \mathbf{U}_n + \Delta t \mathcal{N}\,[t_{n+1}, \mathbf{U}_{n+1}] \tag{5.6}$$

As it is clear, the explicit method only employs the solution at the previous step to find $\mathbf{U}_{n+1}$, whereas in the implicit method $\mathbf{U}_{n+1}$ is a function of both $\mathbf{U}_n$ and $\mathbf{U}_{n+1}$.

A multi-stage method with s stages gets to the approximate solution by using $s - 1$ intermediate steps between n and $n + 1$: the solution becomes

$$\mathbf{U}_{n+1} = \mathbf{U}_n + \Delta t \sum_{k=s_0}^{s} \alpha_k \mathcal{N}\,[t_{n+1-k}, \mathbf{U}_{n+1-k}] \tag{5.7}$$

where s_0 is the starting stage and α_k the coefficients of the linear combination, whose sum must be equal to the unity. The value of s_0 makes the method explicit or implicit: if $s_0 = 0$ the method is implicit, if $s_0 > 0$ it is explicit. Generally speaking, an explicit method is computationally less burdening but its stability is bound to certain conditions, whereas an implicit method, albeit slower, is stable for each time step.

The Unsteady Robust All-around Navier-StOkes Solver (URANOS), developed by Francesco De Vanna as his PhD thesis [44], [37], [38] simulates the behaviour of compressible viscous flows and is capable of dealing with moving bodies immersed in the fluid, at various Mach and Reynolds numbers. URANOS employs a third order explicit Runge-Kutta method to solve the Navier-Stokes equations in their filtered, non-dimensional form. The third-order Runge-Kutta method (RK3) employed in URANOS uses two intermediate *pseudo-solutions* to obtain $\mathbf{U}_{n+1}$ from $\mathbf{U}_n$:

$$\begin{cases} \mathbf{U}_{(1)} = \mathbf{U}_n + \Delta t \mathcal{N}\left[t_n, \mathbf{U}_n\right] \\ \mathbf{U}_{(2)} = \frac{3}{4}\mathbf{U}_n + \frac{1}{4}\mathbf{U}_{(1)} + \frac{1}{4}\Delta t \mathcal{N}\left[t_{(1)} + \frac{1}{2}\Delta t, \mathbf{U}_{(1)}\right] \\ \mathbf{U}_{n+1} = \frac{1}{3}\mathbf{U}_n + \frac{2}{3}\mathbf{U}_{(2)} + \frac{2}{3}\Delta t \mathcal{N}\left[t_{(2)} + \frac{1}{2}\Delta t, \mathbf{U}_{(2)}\right] \end{cases} \tag{5.8}$$

Being this method explicit, its stability depends on the time step chosen: it must be brief enough to grasp the time-variation of the characteristic wave propagation. This criterion, known in the fields of Fluid Dynamics as the CFL, Courant-Friedrichs-Lewy stability condition, is the strictest with respect to convective fluxes; for diffusion phenomena, instead, the FO, Fourier criterion, is employed to ensure the stability of the method. Among all the many different formulations of the CFL-required time step, the one adopted by the maker of the URANOS tool is that of Pirozzoli (2002) [26]

$$\Delta t_{CFL} = CFL \min_{j=1}^{3} \left(\frac{\min\left(\Delta x_j\right)}{\max\left(|u_j| + c\right)} \right) \tag{5.9}$$

where Δx_j is the grid step in the j-th direction, u_j the velocity component in that same direction and c the local speed of sound. Analysis from the fathers of this Runge-Kutta method, Gottlieb and Shu (1998) [27] concluded that valid results are obtained for values of CFL up to 1, while an optimal choice would roughly be $0.5 < CFL < 0.8$. The Fourier criterion instead is defined with

$$\Delta t_{FO} = FO \min \left(\frac{min_j\left(\Delta x_j\right)^2}{\mu_\infty \max\left(\mu\right)}, \frac{\gamma/(\gamma-1)\min\left(\rho\right)min_j\left(\Delta x_j\right)^2}{\lambda_\infty \max\left(\mu\right)} \right) \tag{5.10}$$

In this instance Δx_j is like above, μ is the viscosity, ρ the density, $\mu_\infty = \frac{\sqrt{\gamma}M}{Re}$ the reference viscosity, $\lambda_\infty = \frac{\mu_\infty \gamma}{Pr(\gamma-1)}$ the reference diffusivity and FO the Fourier number, here assumed to be equal to 0.1. Since obviously both criteria for the minimum time step have to be fulfilled, the effective Δt considered in the calculations has been set to

$$\Delta t = \min\left(\Delta t_{CFL}, \Delta t_{FO}\right) \tag{5.11}$$

5.2 Energy-preserving scheme

As far as time is concerned, the advancement is carried out using the Runge-Kutta approach introduced above. In the case of compressible flows, however, in order not to make the simulation blow up, an energy-preserving method developed by Pirozzoli (2010) [28] was employed. This central sixth-order locally conservative method, applied to the nonlinear terms of the Navier-Stokes equations, guarantees that the total kinetic energy is discretely conserved in the limit case of inviscid incompressible flows. By using this approach, there is no need for an artificial viscosity for numerical stabilisation, an in most existing compressible flow solvers. Being

$$\left(\frac{\partial \rho u_j \phi}{\partial x_j} \right)_i \simeq \frac{1}{\Delta x_j} \left(\hat{f}_{i+\frac{1}{2}} - \hat{f}_{i-\frac{1}{2}} \right) \tag{5.12}$$

a convective derivative of a generic transported scalar quantity (1 for the continuity equation, $\{u_i\}_{i=1}^{3}$ for the momentum equations and $H = \gamma/(\gamma-1)p/\rho + u^2/2$ for the total energy equation), a fully split approximation for Equation (5.12) is

$$\frac{\partial \rho u_j \phi}{\partial x_j} = k_1 \frac{\partial \rho u_j \phi}{\partial x_j} + k_2 \left(\rho \frac{\partial u_j \phi}{\partial x_j} + u_j \frac{\partial \rho \phi}{\partial x_j} + \phi \frac{\partial \rho u_j}{\partial x_j} \right) + (1 - k_1 - k_2) \left(\rho u_j \frac{\partial \phi}{\partial x_j} + \rho \phi \frac{\partial u_j}{\partial x_j} + u_j \phi \frac{\partial \rho}{\partial x_j} \right)$$

(5.13)

Here, a conservative approximation is guaranteed if $k_1 = k_2 = 1/4$. The numerical flux linked to the formulation above is given by

$$\hat{f}_{i+\frac{1}{2}} = 2 \sum_{l=1}^{L} a_l \sum_{m=0}^{l-1} \left(\widetilde{\rho, u, \phi} \right)_{i-m,l}$$

(5.14)

where

$$\left(\widetilde{\rho, u, \phi} \right)_{i,l} = \frac{1}{8} \left(\rho_i + \rho_{i+l} \right) \left(u_i + u_{i+l} \right) \left(\phi_i + \phi_{i+l} \right)$$

(5.15)

is the discrete averaging operator for the transported variable ϕ. In this case (see [28]) the formal order of accuracy is maximised by $a_1 = 1/60$, $a_2 = -3/20$, $a_3 = 3/4$.

5.3 Grid

Having defined the closure equations (1.8, 1.9), a spatial discretisation of the channel must be provided. The idea of the turbulent channel consists of a flow moving between two indefinitely extended parallel walls. In the stream-wise direction, this is implemented by making the flow recirculate, whereas the y and z directions have to be bounded and wide enough to accommodate the larger vortical structures which become energetically relevant at sufficiently high Reynolds numbers. In the wall-normal direction, the most important and computationally most challenging one, an hyperbolic grid has been implemented: the nodes are increasingly more packed near the wall and spaced towards the center of the channel. The goal is obviously to better capture the dynamics of the fluid in the turbulent boundary layer. The law for the distribution of the grid nodes in the y-direction is [44]

$$y(\xi) = 1 + \frac{\tanh\left[\alpha\left(\xi - 1\right)\right]}{\tanh\left(\alpha\right)}$$

(5.16)

where α is a parameter linked to the stretching of the grid and ξ is a coordinate on the uniform grid that allows to transform the computed data to fit them into the hyperbolic grid. On the other hand, stream- and span-wise grid distributions are uniform and the number of points is designed to compromise between resolution and computational load.
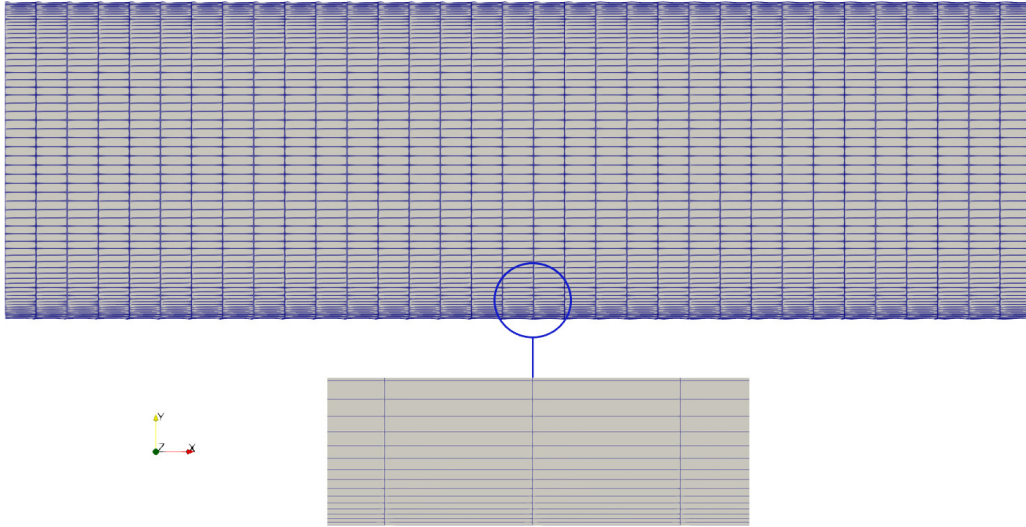
Figure 5.1: Distribution of the channel cells in the $Re_\tau = 215$ case, following a uniform pattern in the stream-wise direction and Equation (5.16) in the wall-normal direction (top); detail of the cell distribution near the bottom wall (bottom).

In Figure 5.1 the bottom part represents the wall, while the left and right parts are the inlet and outlet respectively (see Figure 5.2 also). In the present study the number of points adopted is $32 \times 64 \times 32$ for the case $Re_\tau = 215$ and $80 \times 160 \times 80$ for $Re_\tau = 500$ in respectively the x, y and z directions; the dimensions of the channel are $2\pi \times 2 \times \pi$. The reason behind this is that in the $Re_\tau = 500$ case, the vortices will have smaller dimensions so a better resolution is required.
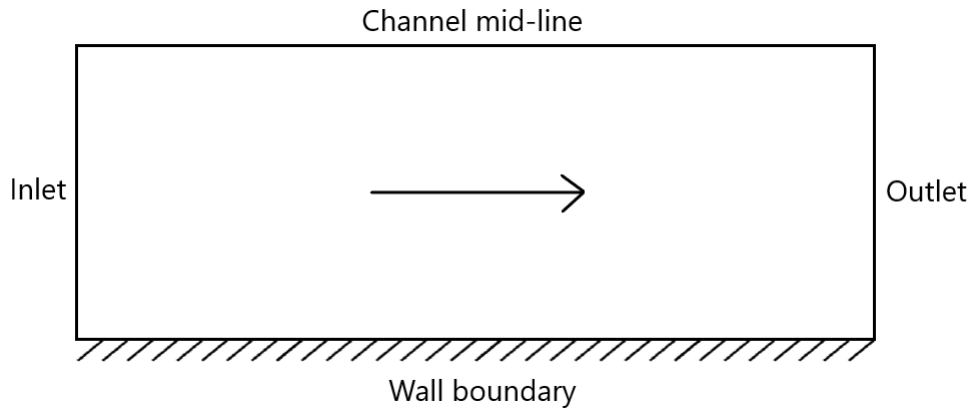
Figure 5.2: Boundaries of the simulation domain.

5.4 Boundary conditions

In order to treat and solve the Navier-Stokes equations a set of boundary conditions must be specified. At the bottom of the domain, where the wall is located, the compressible case requires not only the standard boundary condition such as isothermal and no-slip wall, but also a set of so called Navier-Stokes characteristic boundary conditions (NSCBC), which still represent a challenge in the study of compressible flows; this is mainly due to acoustic phenomena: the "numerical" pressure waves tend to reflect at the boundaries of the channel and ascend the channel even if the flow is supersonic, influencing the solution and further complicating the problem. Let's consider a one-dimensional Navier-Stokes problem, for the sake of simplicity, in the generalised form of

$$\frac{\partial \mathbf{U}}{\partial t} = -\frac{\partial \mathbf{F}(\mathbf{U})}{\partial x} \tag{5.17}$$

where $\mathbf{U} = \{u_k\}_{k=1}^n$ is a set of variables and $\{\mathbf{F}^{(j)}(\mathbf{U})\}_{j=1}^3$ their fluxes. Following the theory of hyperbolic PDEs, this system can be rewritten in its primitive form as

$$\frac{\partial \mathbf{U}}{\partial t} = -\mathbf{J}\frac{\partial \mathbf{U}}{\partial x} \tag{5.18}$$

$$\frac{\partial \mathbf{U}}{\partial t} = -\mathbf{R}_x \mathbf{\Lambda}_x \mathbf{L}_x \frac{\partial \mathbf{U}}{\partial x} \tag{5.19}$$

where $\mathbf{\Lambda}_x$ is the diagonal matrix containing the eigenvalues $\left\{\lambda_k^{(j)}\right\}_{k=1}^n$ of the Jacobian matrices $J_{ik}^{(j)} = \frac{\partial \mathbf{F}_i^{(j)}(\mathbf{U})}{\partial u_k}$ and $\mathbf{R}_x$ and $\mathbf{L}_x$ the right and left eigenvectors associated to those matrices. The five characteristic waves associated with the flux component can be written as

$$\mathcal{L}_x = \mathbf{\Lambda}_x \mathbf{L}_x \frac{\partial \mathbf{U}}{\partial x} = \begin{cases} \lambda_1 \left(\frac{\partial p}{\partial x} - \rho c \frac{\partial u}{\partial x}\right) \\ \lambda_2 \left(c^2 \frac{\partial \rho}{\partial x} - \frac{\partial p}{\partial x}\right) \\ \lambda_3 \frac{\partial v}{\partial x} \\ \lambda_4 \frac{\partial w}{\partial x} \\ \lambda_5 \left(\frac{\partial p}{\partial x} + \rho c \frac{\partial u}{\partial x}\right) \end{cases} \tag{5.20}$$

where c is the velocity of the wave. Therefore

$$\frac{\partial \mathbf{U}}{\partial t} = -\mathbf{R}_x \mathcal{L}_x(\mathbf{U}) \tag{5.21}$$

If $\mathbf{U}$ is replaced with the actual values taken from the Navier-Stokes equations, (5.21) reads

$$\begin{cases} \frac{\partial \rho}{\partial t} = -d_1 \\ \frac{\partial \rho u_1}{\partial t} = -u_1 d_1 - \rho d_3 \\ \frac{\partial \rho u_2}{\partial t} = -u_2 d_2 - \rho d_4 \\ \frac{\partial \rho u_3}{\partial t} = -u_3 d_3 - \rho d_3 \\ \frac{\partial \rho E}{\partial t} = -\frac{1}{2} u_i u_i d_1 - \frac{d_1}{\gamma-1} - \rho(u_1 d_3 + u_2 d_4 + u_3 d_5) \end{cases} \tag{5.22}$$

29

with

$$d = \begin{cases} \frac{1}{c^2}\left(\mathcal{L}_2 + \frac{1}{2}\left(\mathcal{L}_1 + \mathcal{L}_5\right)\right) \\ \frac{1}{2}\left(\mathcal{L}_1 + \mathcal{L}_5\right) \\ -\frac{1}{2\rho c}\left(\mathcal{L}_1 - \mathcal{L}_5\right) \\ \mathcal{L}_3 \\ \mathcal{L}_4 \end{cases} \tag{5.23}$$

According to Yoo et al. (2007) [29], some assumptions can be made about the characteristic waves $\mathcal{L}_x$ (see [44]), based on the different scenarios.

Regarding the inflow and outflow conditions, in this instance there is a periodicity condition imposed to the flow in the x and z directions: the properties of the inlet flow are exactly the same as the outlet flow. This, in conjunction with the forcing mechanism, ensures the proper motion of the fluid within the channel.

6 Results

In this Chapter the results of the numerical simulations are presented and confronted. The simulations have been conducted employing two different values for the friction Reynolds number Re_τ, 215 and 500 at a Mach number of 1.5 for all. The benchmark for every graph in this chapter is the incompressible data obtained by Vreman and Kuerten (2014) [30] with a high-resolution long-time DNS re-simulation of a classic case studied mainly by Kim and Moser ([31], [32]). This particular set of data has been treated like an incompressible "absolute" non-dimensional reference and therefore not subject to any transformations, unlike the compressible data acquired from the numerical simulations performed for this study. Moreover, visual representation of the different fields will be provided, giving an idea of how the flow conducts itself in the channel and what the differences between the various implementations are.

Before performing the simulations presented above, the first step has been to validate the (already extensively tested [44], [37], [38]) URANOS through an analysis of the ILES, DSMG, and WALE models at $M_\infty = 0.1$ and $M_\infty = 0.3$ and $Re_\tau = 180$ (Figure 6.1) using a van Driest transformation, i.e. in a situation that would theoretically be very similar to an incompressible one, in accordance with the LES model inherent accuracy. From Figure (6.1) a tendency can be seen for all models to accurately collapse to the incompressible data in the near-wall region, whereas different behaviours are observed towards the center of the channel. The dashed lines represent the law-of-the-wall $u^+ = y^+$ and the logarithmic law $u^+ = 5.2 + \frac{\log(y^+)}{0.41}$; the latter provides the theoretically correct slope of the curve approaching the center of the channel.

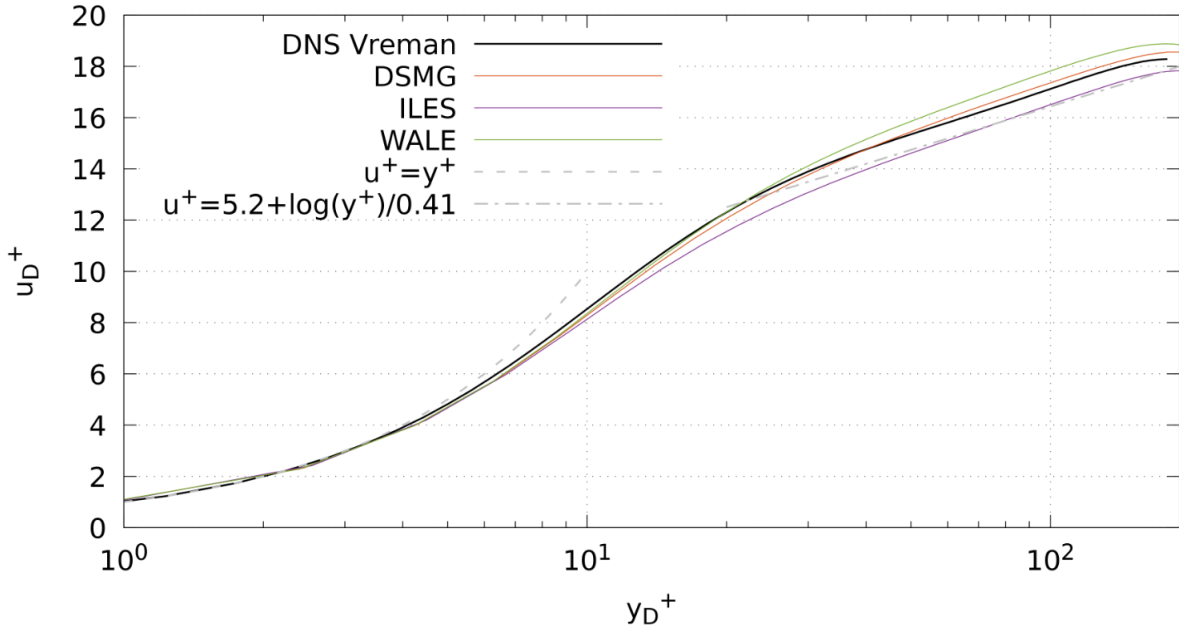

Figure 6.1: Comparison of van Driest transformed mean velocity with different methods at $M_\infty = 0.3$ and $Re_\tau = 180$.
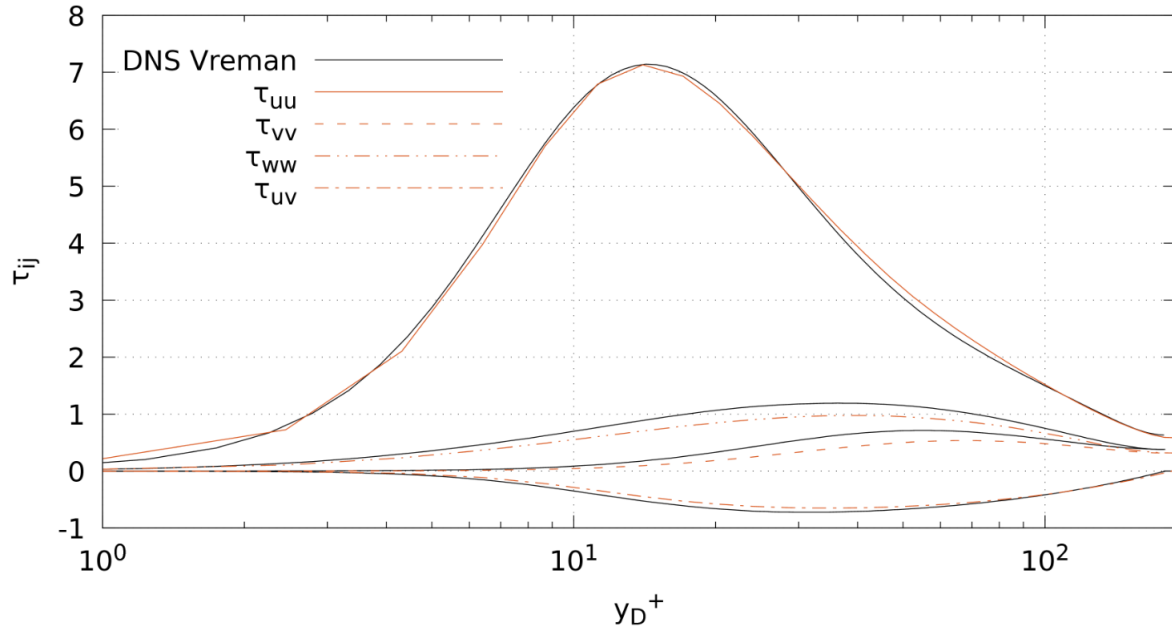
Figure 6.2: Comparison of Smagorinsky Reynolds stresses at $M_\infty = 0.3$ and $Re_\tau = 180$ with DNS data by Vreman (2014) [30].

The same procedure has been adopted with the Reynolds stresses, of which the Smagorinsky results are presented in Figure (6.2). Again, the results are in sufficient accordance with the DNS, especially the most relevant stream-wise Reynolds stress τ_{uu}.

6.1 Mean velocity fields

In this section are the velocity fields obtained by transforming the physical fields with the van Driest method in the case of $Re_\tau = \frac{\rho_w u_\tau h}{\mu_w} = 215$, i.e. the less turbulent flow. As per Table 1, the van Driest transformation for the mean velocity is given by Equation (4.6). Figure 6.3 shows the curves resulting from the different methods. It appears clear that the four methods slightly but visibly undershoot the theoretical linear distribution of the viscous sublayer beyond $y_D^+ \approx 3$ and they all systematically overshoot the incompressible distribution away from the wall, the crossing occurring at $y_D^+ \approx 30$, in accordance with the DNS results of Modesti, Pirozzoli [17]. The percent error, defined as $\varepsilon_r = \left| \frac{\bar{u}_{LES} - \bar{u}_{DNS}}{\bar{u}_{DNS}} \right| \cdot 100$ and calculated at $y^+ = 120$, is around 10% for the DSMG, MXTS and WALE methods, while it stands at 8.6% for the unresolved method.

In Figure 6.4 the same data resulting from the simulations was transformed with the method implemented by Trettel and Larsson (4.21). This approach seems to solve the undershooting problem in the near-wall region, up to $y_D^+ \approx 10$, whereas it again overshoots the DNS results in the outer layer, although less severely than the van Driest mean velocity fields. Because van Driest was designed for a turbulent channel with adiabatic walls and the channel used in this study has isothermal walls instead,
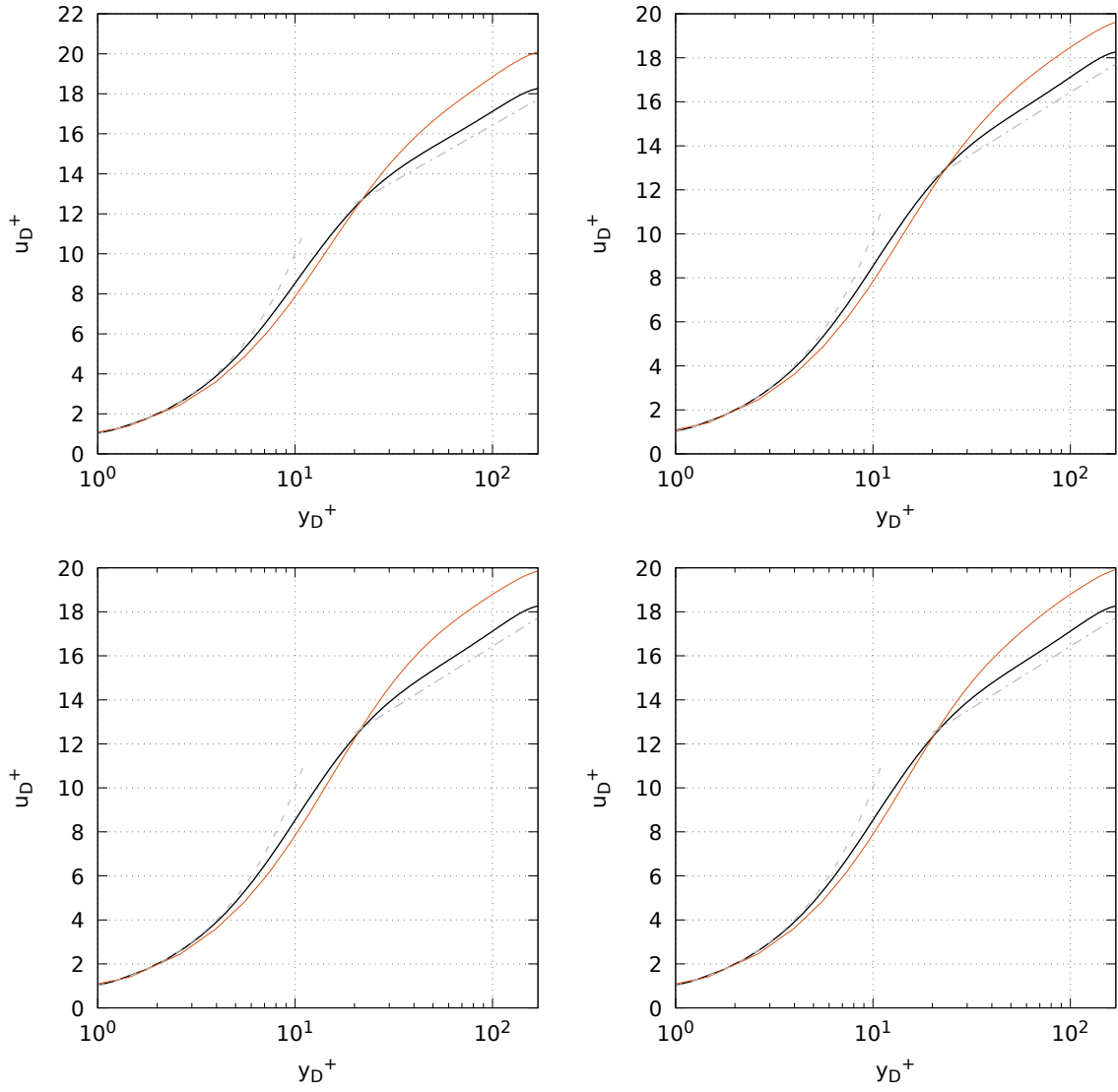
Figure 6.3: Mean velocity profiles (orange) transformed according to van Driest at $M_\infty = 1.5$ and $Re_\tau = 215$ using the Smagorinsky (DSMG) model (top left), the unresolved (ILES) approach (top right), mixed time scale (MXTS) model (bottom left) and wall-adapted large-eddy (WALE) model (bottom right). The black lines denote the DNS results by Vreman and the dashed lines represent the law-of-the-wall and the logarithmic law respectively.
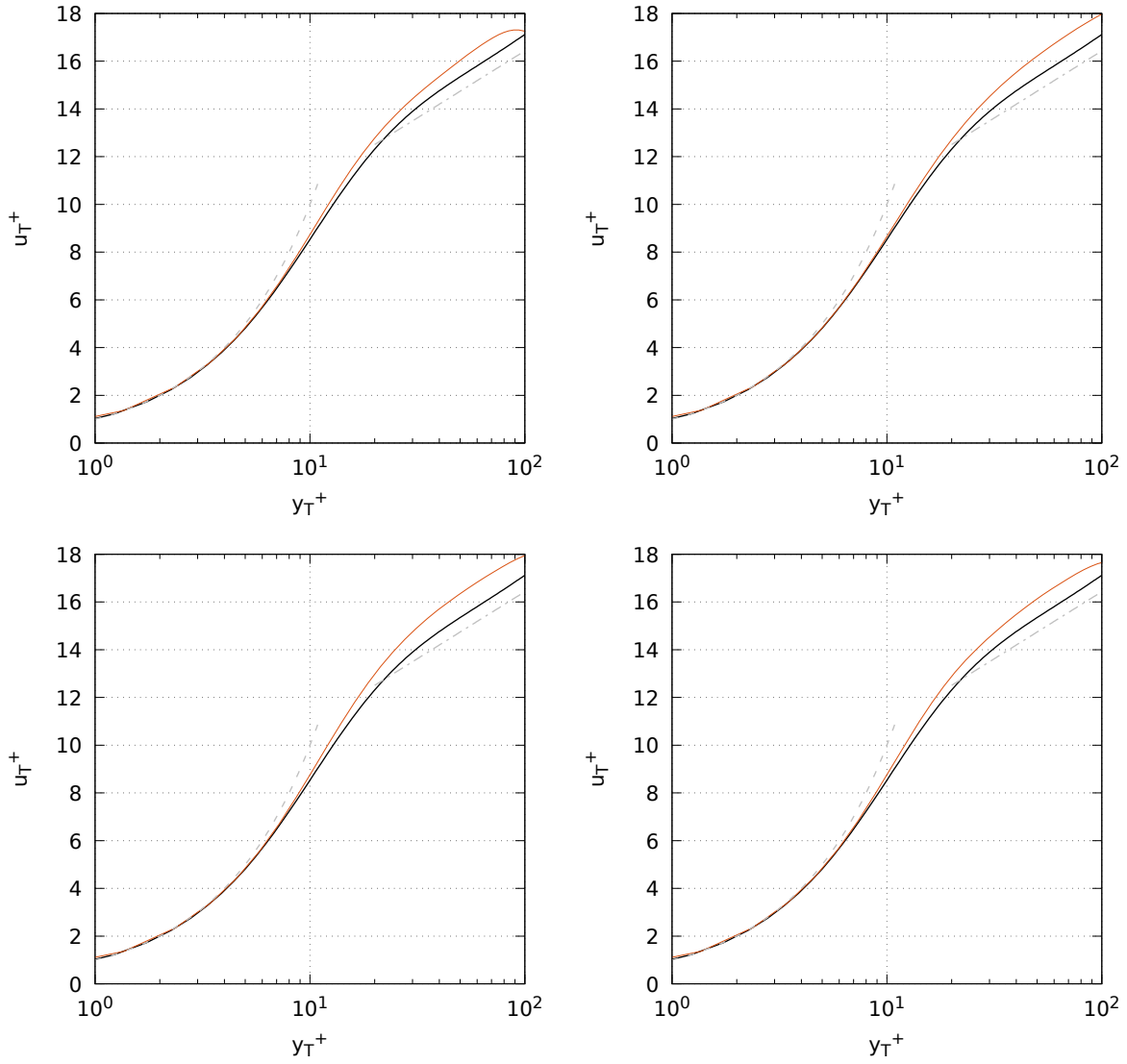
Figure 6.4: Mean velocity profiles, transformed according to Trettel and Larsson at $M_\infty = 1.5$ and $Re_\tau = 215$ using the Smagorinsky (DSMG) model (top left), the unresolved (ILES) approach (top right), mixed time scale (MXTS) model (bottom left) and wall-adapted large-eddy (WALE) model (bottom right). The black lines denote the DNS results by Vreman and the dashed lines represent the law-of-the-wall and the logarithmic law respectively.

the van Driest transformation badly represents the actual velocity in the whole viscous wall region; the more "physically-justified" transformation introduced by Trettel and Larsson, based on the equilibrium of stresses, works much better near the wall. In fact, the percent error is between 4.9% (WALE) and 6.7% (MXTS), while the DSMG and ILES methods yield an error of 5% and 6% respectively, at $y^+ = 70$.

In the case of a more turbulent flow, $Re_\tau = 500$, the subgrid-scale becomes more important, especially in the region near the cooled, isothermal wall. For this reason the van Driest transformation is expected to perform worse than the Trettel and Larsson one; in Figure 6.5 the curves obtained corroborate this hypothesis: they lose strict adherence to the Vreman data at $y_D^+ \approx 3$ the maximum error occurring at roughly $y^+ = 15$, where it stands around 7% for the WALE, 8% for the DSMG, 8.5% for the MXTS and 9% for the ILES model. This can be explained by the fact that up to $y^+ \approx 3$ the flow is still greatly affected by the presence of the wall, albeit non-adiabatic, and akin to an incompressible one. While the unresolved model performed well at the lower friction Reynolds number, and actually arguably better than its turbulence-modelling counterparts, at $Re_\tau = 500$ the modelling starts to yield its fruits not only in the overlap layer but towards the center of the channel as well, where the percent error is 0.06%, 2.28%, 0.64% and 1.35% for the DSMG, ILES, MXTS and WALE methods respectively ($y^+ = 100$). The acute overshooting with respect to the incompressible DNS data by Vreman is not observed in this case and the slope in the outer layer is more similar to the DNS.

Figure 6.6 shows the same results, post-processed using the Trettel and Larsson transformation. This approach makes for a good collapse up to $y_D^+ \approx 10 \Rightarrow y \approx 0.02$, fixing the problem in the overlap layer with respect to the van Driest-transformed data; the four models go back to undershooting the incompressible data towards to the center line of the channel. The four methods yield similar results there, the percent errors being 4%, 3.25%, 1.5% and 2% respectively. In this case the Smagorinsky model performs worse than the other two resolved models not only in terms of accuracy to the DNS data but also in terms of time.

From Figure 6.7 gives an idea on how the Mach number behaves along the wall-normal direction of the channel: at a lower friction Reynolds number, the dimension of the low-speed boundary layer is significantly larger than in the case at $Re_\tau = 500$; in the latter case the stronger turbulence makes for a smoother transition from the no-slip condition at the wall location and the fully developed flow at the center of the channel. Figure 6.8 offers a visual representation of the velocity in for both $Re_\tau = 215$ and $Re_\tau = 500$: here the most evident effect of the friction Reynolds number seems to be linked to the dimension of the vortices, smaller in the case of $Re_\tau = 500$. Another interesting aspect is the effective dimension of the boundary layer, which appears to be thinner in the second image. Figure 6.9 shows the behaviour of the fluid in different directions and in different areas of the channel; as one would expect, in the more turbulent flow the nominal mean velocity is reached closer to the wall since the viscous length scale is inversely proportional to Re_τ. The vortices in Figure 6.10 were generated using iso-contours with the Q-criterion $Q = 1$ and $Q = 3.5$ as parameters, respectively. The Q-criterion, formulated by Hunt, Wray and Moin (1988) [39] was the first three-dimensional vortex criterion. For a three-dimensional velocity field $\bar{u}(x, t)$ whose gradient decomposition is

$$\nabla \bar{u} = S + \Omega \tag{6.1}$$

where $S = \frac{1}{2} \left[\nabla \bar{u} + (\nabla \bar{u})^T \right]$ is the rate-of-strain tensor and $\Omega = \frac{1}{2} \left[\nabla \bar{u} - (\nabla \bar{u})^T \right]$ the vorticity tensor, the Q-criterion is defined as

$$Q = \frac{1}{2} \left[|\Omega|^2 - |S|^2 \right] > 0 \tag{6.2}$$
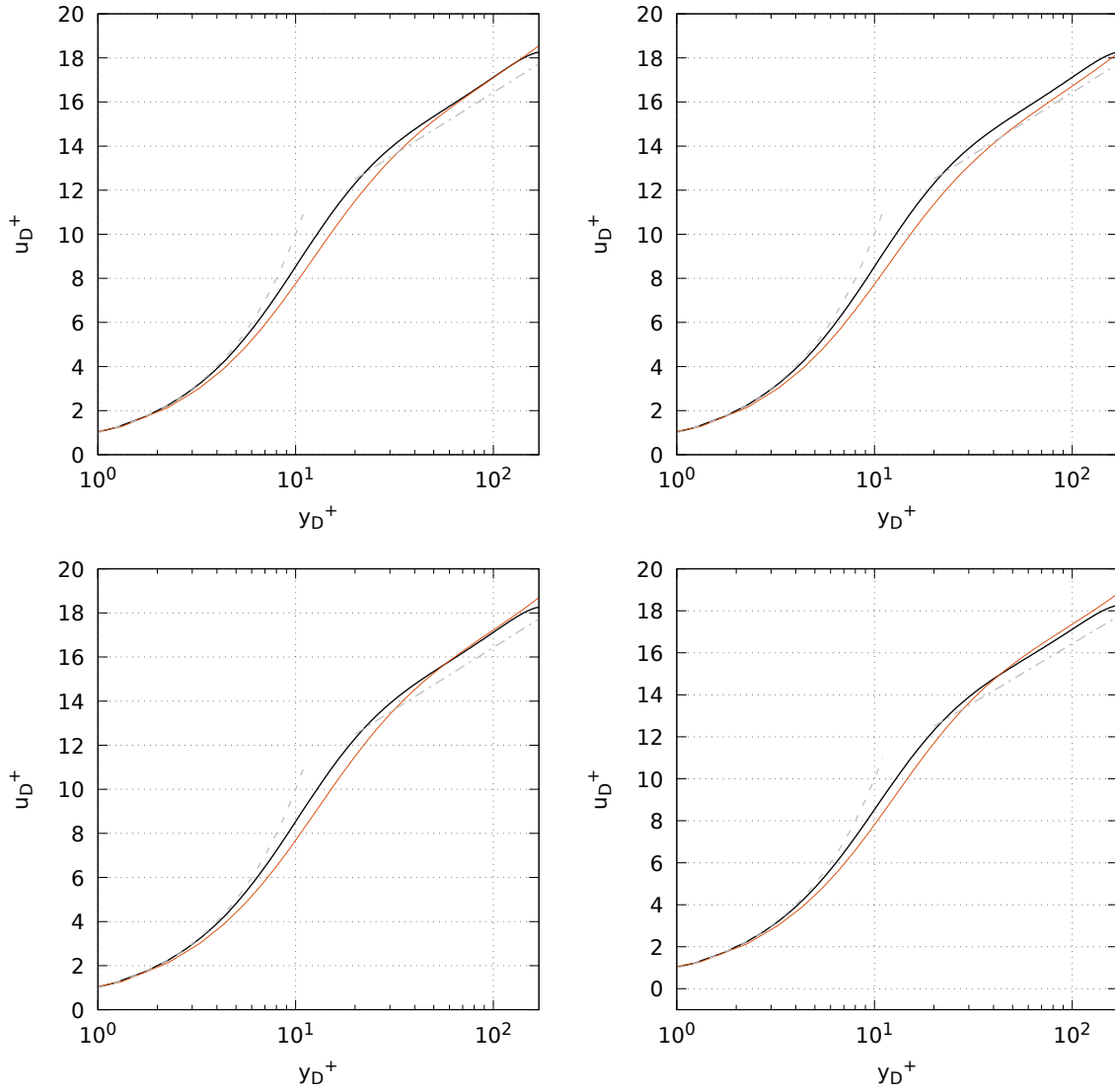
Figure 6.5: Mean velocity profiles, transformed according to van Driest at $M_\infty = 1.5$ and $Re_\tau = 500$ using the Smagorinsky (DSMG) model (top left), the unresolved (ILES) approach (top right), mixed time scale (MXTS) model (bottom left) and wall-adapted large-eddy (WALE) model (bottom right). The black lines denote the DNS results by Vreman and the dashed lines represent the law-of-the-wall and the logarithmic law respectively.
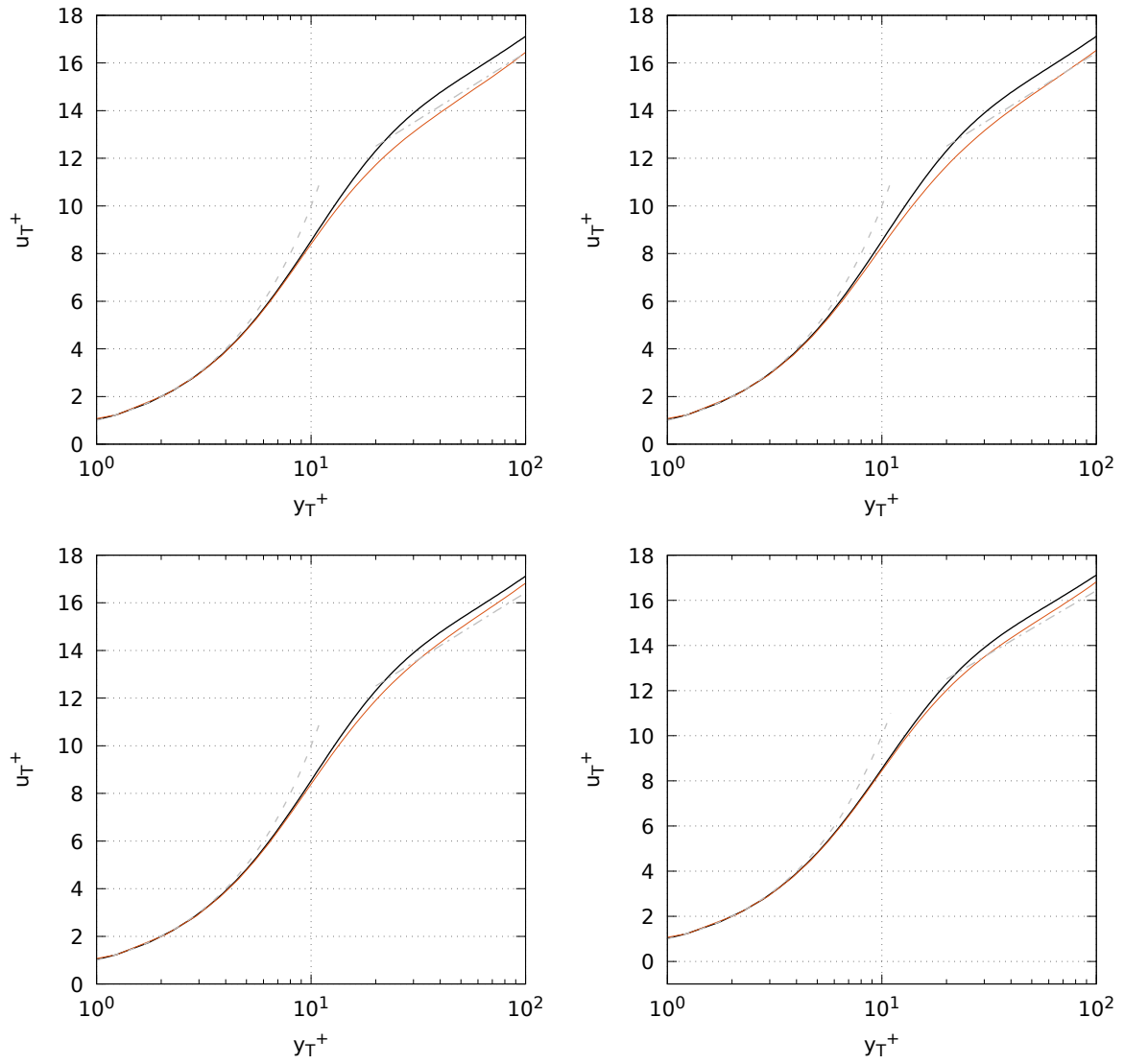
Figure 6.6: Mean velocity profiles, transformed according to Trettel and Larsson at $M_\infty = 1.5$ and $Re_\tau = 500$ using the Smagorinsky (DSMG) model (top left), the unresolved (ILES) approach (top right), mixed time scale (MXTS) model (bottom left) and wall-adapted large-eddy (WALE) model (bottom right). The black lines denote the DNS results by Vreman and the dashed lines represent the law-of-the-wall and the logarithmic law respectively.

According to Hunt, Wray and Moin, a vortex is defined as a spatial region where the Euclidean norm of the vorticity tensor Ω dominates that of the rate of strain S [40].
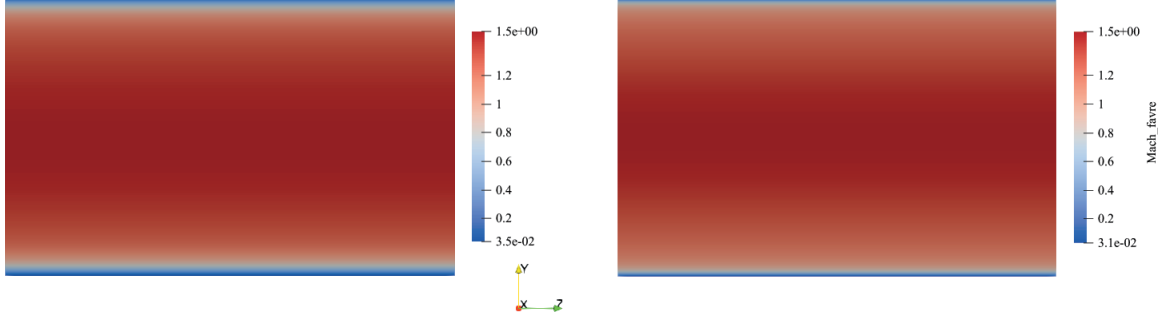

Figure 6.7: Slice representing the behaviour of the Mach number with the mixed time scale (MXTS) model at $M_\infty = 1.5$ and $Re_\tau = 215$ (left) and $Re_\tau = 500$ (right).
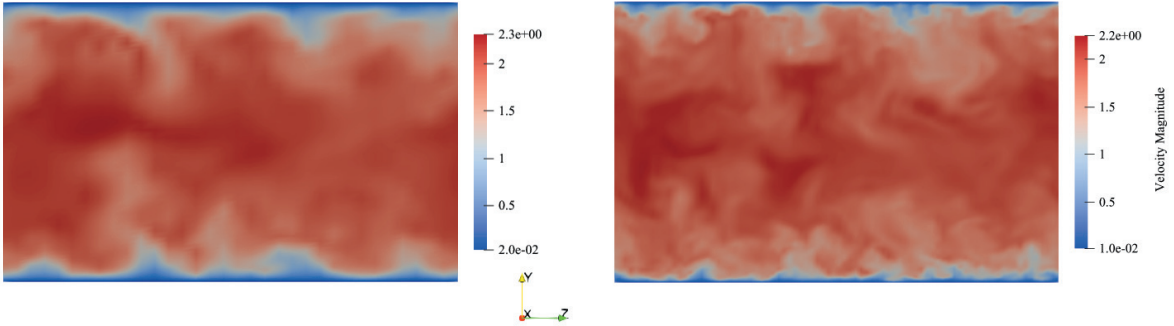

Figure 6.8: Slice of the mean velocity fields obtained with the mixed time scale (MXTS) model at $M_\infty = 1.5$ and $Re_\tau = 215$ (left) and $Re_\tau = 500$ (right).

6.2   Reynolds stresses

As can be seen in Table 1, the Trettel and Larsson transformation for the Reynolds stresses is the same as the van Driest one, therefore only the latter will be included in this Section, as per Equation (6.3)

$$\tau_{Dij} = \frac{\bar{\rho}}{\rho_w}\tau_{ij} \tag{6.3}$$

In Figures 6.11, 6.12 the transformed Reynolds stresses in comparison with the data by Vreman are shown.
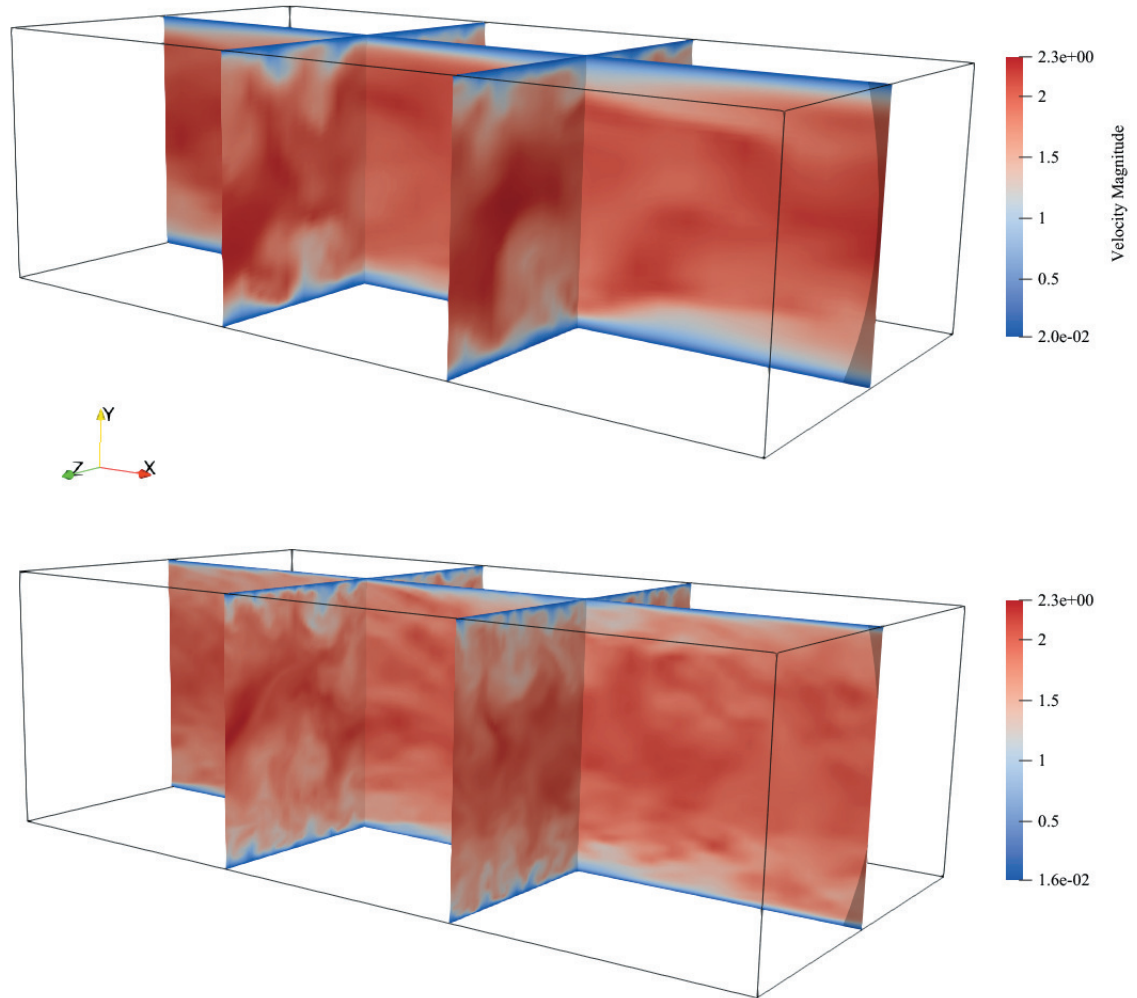
Figure 6.9: Visual representation of different slices of the mean velocity fields with the mixed time scale (MXTS) model at $M_\infty = 1.5$ and $Re_\tau = 215$ (top) and $Re_\tau = 500$ (bottom).
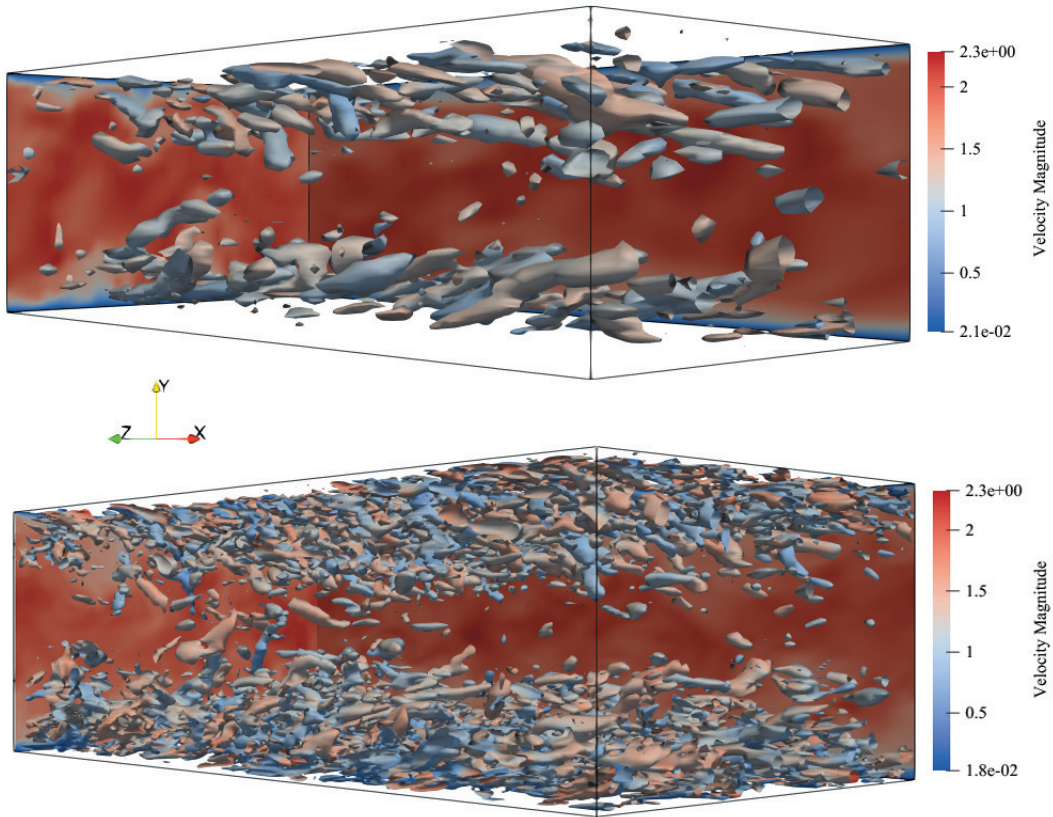
Figure 6.10: Visual representation of iso-contours vortices obtained employing the Q-criterion with the mixed time scale (MXTS) model at $M_\infty = 1.5$ and $Re_\tau = 215$ (left) and $Re_\tau = 500$ (right).
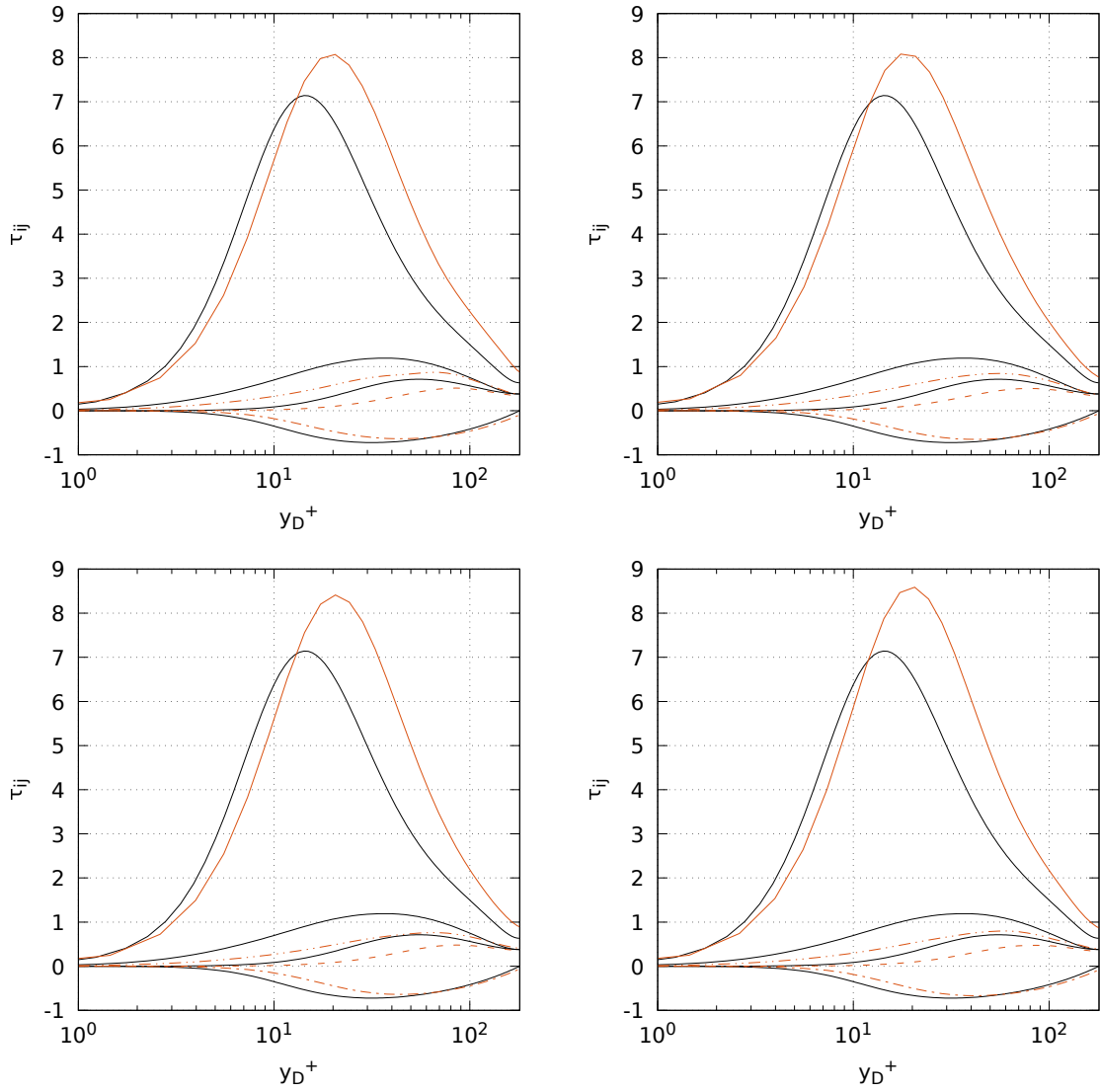
Figure 6.11: Reynolds stresses (orange) transformed according to van Driest at $M_\infty = 1.5$ and $Re_\tau = 215$ using the Smagorinsky (DSMG) model (top left), the unresolved (ILES) approach (top right), mixed time scale (MXTS) model (bottom left) and wall-adapted large-eddy (WALE) model (bottom right). The black lines denote the DNS results by Vreman.

In the case of $Re_\tau = 215$ the results are not overwhelmingly accurate. In fact, a clear mismatch between LES scaled compressible stresses and DNS data in both amplitude and shift in the position of the peaks can be observed towards the middle of the channel for all curves, whereas closer agreement is found in the near-wall region. Modesti and Pirozzoli (2016) [17], whose results are in agreement with the ones in this study, show that a better collapse on the incompressible curve is achieved adopting the Brun (2008) [20] transformation in both peak amplitude and off-wall position. The Brun transformation for the Reynolds stresses reads

$$\tau_{Bij} = \frac{\bar{\rho}}{\rho_w} \left(\frac{y}{y_B} \frac{\mu_w}{\mu} \right)^2 \tau_{ij} \tag{6.4}$$

where the Brun coordinate y_B is given by

$$y_B = \int_0^y \frac{\overline{\rho_w}}{\bar{\rho}} \frac{\overline{\nu_w}}{\bar{\nu}} dy \tag{6.5}$$

As Modesti and Pirozzoli point out, Brun's transformations seems to fail too at higher Mach numbers, where the peak maintains its accuracy in terms of magnitude but it is clearly shifted with respect to the incompressible data.

For $Re_\tau = 500$, Figure 6.12 there is in all methods a generally better collapse on the incompressible data in the near-wall region and the peaks are more coherently placed, but the y^+ coordinate looks more and more "stretched" towards the center of the channel, indicating that the van Driest coordinate scaling $y_D^+ = y\rho_w \sqrt{\tau_w/\rho_w}/\mu_w$ is more appropriate for lower Re_τ. The Trettel and Larsson coordinate transformation (4.18) mitigates the problem but tends to behave in the same manner.
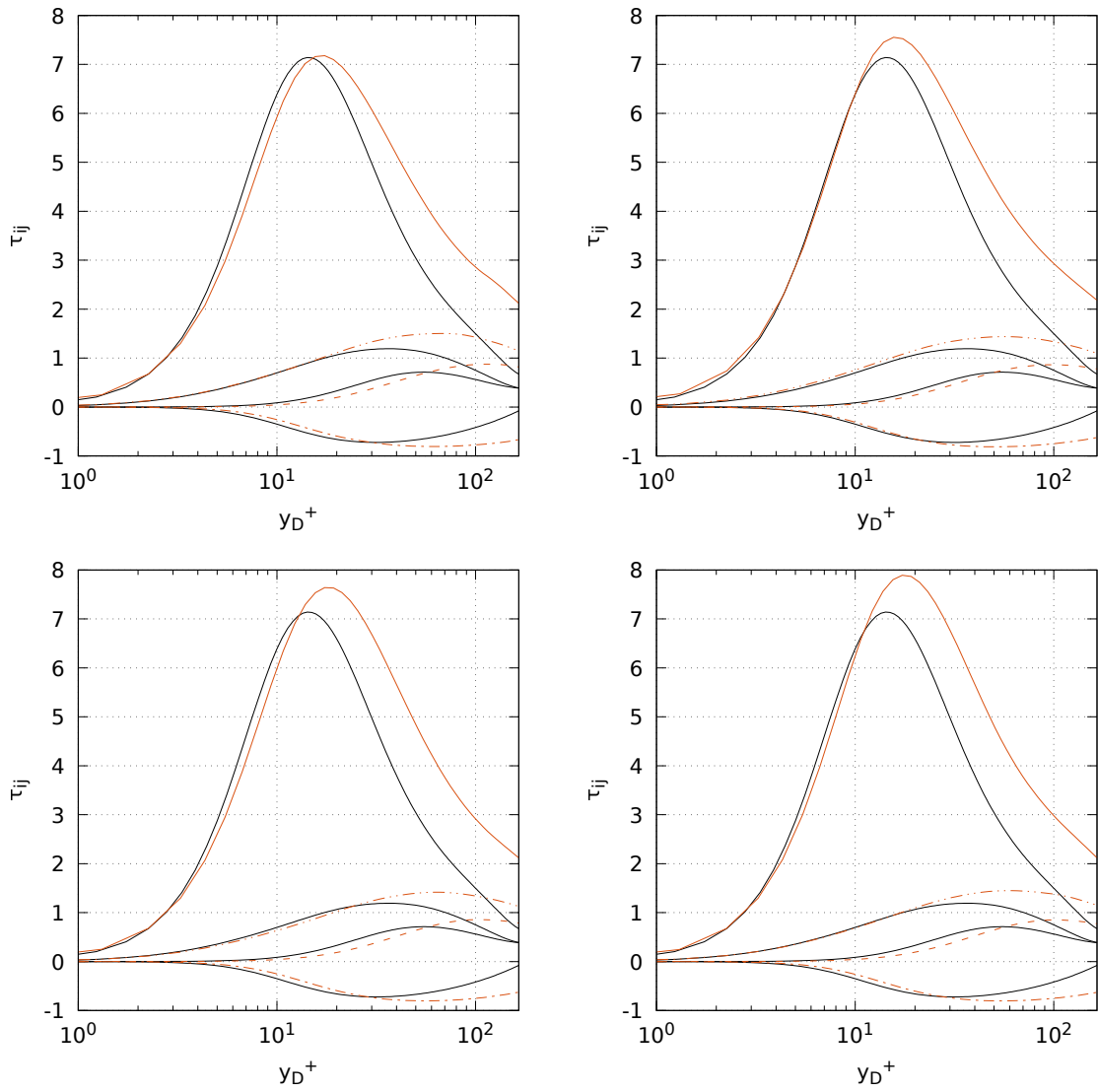
Figure 6.12: Reynolds stresses (orange) transformed according to van Driest at $M_\infty = 1.5$ and $Re_\tau = 500$ using the Smagorinsky (DSMG) model (top left), the unresolved (ILES) approach (top right), mixed time scale (MXTS) model (bottom left) and wall-adapted large-eddy (WALE) model (bottom right). The black lines denote the DNS results by Vreman.

6.3 Mean temperature

A correct assessment of the temperature is of great importance especially in the case of isothermal walls, as it is necessary to define and predict the heat transfer coefficient at the wall q_w. Moreover, an accurate temperature-velocity relation is critical to perform the inverse of the compressibility transformations to determine the mean velocity profile in the non-transformed space. The temperature-velocity traditionally used, derived by Walz (1959) [33]

$$\frac{T}{T_w} = 1 + \frac{T_r - T_w}{T_w}\frac{\bar{u}}{\bar{u}_e} - r\frac{\gamma - 1}{2}M_e^2\frac{T_e}{T_w}\left(\frac{\bar{u}}{\bar{u}_e}\right)^2 \tag{6.6}$$

where

$$T_r = T_e\left(1 + r\frac{\gamma - 1}{2}M_e^2\right) \tag{6.7}$$

is the recovery temperature, $r = 0.89$ is the recovery factor and the subscript e indicates the value at the channel centerline. Walz derived this formulation from a simplified form of the energy equation, obtained by making various assumptions such as the neglect of turbulent dissipation and and pressure-strain terms. Further tests by Pirozzoli et al. (2004) [34] at $M = 2.25$ and by Duan et al. (2010) [35] at $M = 5$ found good agreement between Walz's formulations and DNS data at different (fixed) wall temperatures but differences would arise in the case of isothermal walls, where an alternative formulation of the temperature-velocity formulation which considered the heat transfer was required (see [17]). For this reason, Zhang et al. (2014) [36] developed an alternative temperature-velocity relation which introduced a generalised recovery factor that explicitly takes into account the wall heat flux q_w in the presence of non-adiabatic walls

$$\frac{T}{T_w} = 1 + \frac{T_{rg} - T_w}{T_w}\frac{u}{u_e} + \frac{T_e - T_{rg}}{T_w}\left(\frac{u}{u_e}\right)^2 \tag{6.8}$$

where

$$T_{rg} = T_e + r_g\frac{u_e^2}{2c_p} \tag{6.9}$$

and

$$r_g = \frac{2c_p(T_w - T_e)}{u_e^2} - \frac{2Prq_w}{u_e\tau_w} \tag{6.10}$$

This formulation coincides with the Walz relation in the case of adiabatic walls, i.e. $q_w = 0$; Figure 6.13 shows the typical trend of the temperature curve with respect to u/u_e in the case of $Re_\tau = 500$ with a Smagorinsky approach. Figures 6.14 and 6.15 represent the temperature fields, where the difference between the cooled wall regions and the rest of the channel is very evident; the core temperature is reached very close to the boundary.
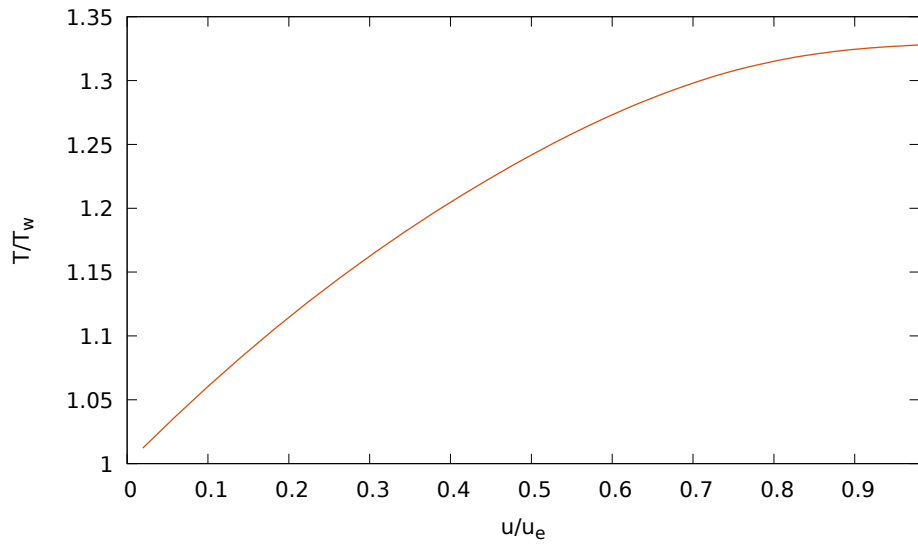
Figure 6.13: Temperature profile against relative velocity u/u_e at $M_\infty = 1.5$ and $Re_\tau = 500$ using the Smagorinsky (DSMG) model.
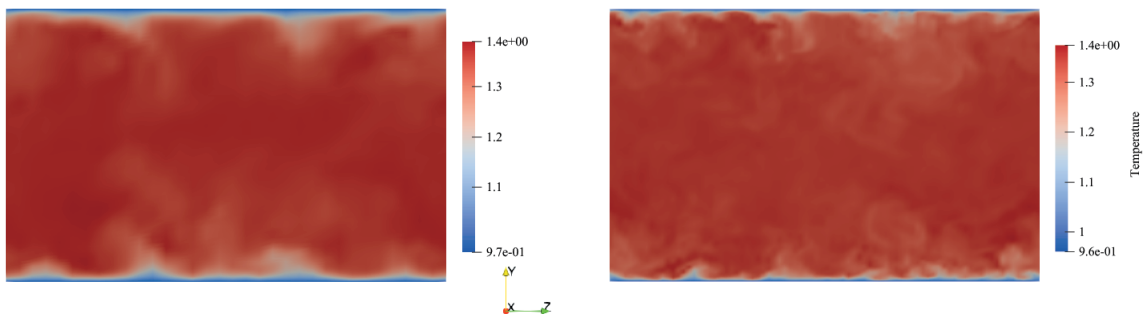

Figure 6.14: Slice of the temperature fields at the outlet of the channel at $M_\infty = 1.5$ and $Re_\tau = 215$ (left) and $Re_\tau = 500$ (right) using the mixed time scale (MXTS) model.

Figure 6.15: z-normal slice of the temperature fields at the side of the channel at $M_\infty = 1.5$ and $Re_\tau = 215$ (top) and $Re_\tau = 500$ (bottom) using the mixed time scale (MXTS) model.

7 Conclusions

The results presented in this work, compared to the incompressible DNS data, further confirm the role of the van Driest transformation of Section 4.1 as an overall inaccurate tool for representing the full inner-layer mean velocity profile, especially in the presence of a wall heat flux. On the other hand, the relatively new and more "coherently-derived" Trettel and Larsson transformation discussed in Section 4.2 yields an improvement as it more faithfully represents the profiles in the channel for both DNS and LES, especially closer to the wall. However, a sufficiently accurate compressibility transformation has yet to be found for the LES of Reynolds stresses, even though the transformation by Brun et. al (2008) [20] seems to yield better collapse to the incompressible data [17]. For what concerns the temperature evaluation, the formulation by Zhang et al. (2014) [36] has been shown to work satisfactorily [17].

The DNS of Kim, Moin and Moser (1984, 1986) was implemented using relatively few grid points (128x65x128) due to the technological hindrance they faced. The DNS carried out by Vreman (2014) [30], based on the historical one and used as the main reference point in this work employed a turbulent channel model with $512 \times 256 \times 256$ grid points, i.e. roughly $3.355 \cdot 10^7$ total points in the domain. Modesti and Pirozzoli (2016) [17] imagined many different scenarios in terms of Mach number, friction Reynolds number and grid points; the grid points distributions they used for their $6\pi h \times 2h \times 2\pi h$ turbulent channel ranged from $120 \times 180 \times 120$ (i.e. $2.592 \cdot 10^6$) points for the most coarse to $2048 \times 512 \times 1024$ for the finest (roughly 10^9 total points). It is in the aspect of sheer grid point number that LES have their strongest ally. The simulations carried out in this work using the URANOS solver employed two grid point distributions, based on the friction Reynolds number: for the case with $Re_\tau = 215$, as stated in Section 5.3, the number of grid points was $32 \times 64 \times 32$ for a grand total of 65536 points, and $80 \times 160 \times 80$ for $Re_\tau = 500$, with $1.024 \cdot 10^6$ points in the channel domain, which is less than half the grid points with respect to the coarsest configuration used by Modesti and Pirozzoli.

Considering the overall accuracy of the simulations, especially at $Re_\tau = 500$ (percent error within 2% for the MXTS and WALE models transformed with Trettel and Larsson), together with the clear advantage in terms of computational time, the LES approach may be worth using in the turbulent channel scenario, provided a more fitting transformation for the Reynolds stresses is formulated.

References

[1] Prandtl, L. (1925). Uber die ausgebildete Turbulenz, *ZAMM.*

[2] von Kármán, Th. (1930). Mechanische Ähnlichkeit und Turbulenz.

[3] Mizuno, Y. , Jiménez, J. (2011). Mean velocity and length-scales in the overlap region of wall-bounded turbulent flows. *Phys. Fluids 23* (8).

[4] Pirozzoli, S. (2012). On the size of the energy-containing eddies in the outer turbulent wall layer. *Journal of Fluid Mechanics 702*, 521–532.

[5] De Vanna, Francesco (2019). A high-resolution fully compressible Navier-Stokes solver for analysis of moving objects at high Mach numbers.

[6] Smagorinsky, J. (1963). General Circulation Experiments with the Primitive Equation I the Basic Experiment. *Monthly Weather Review*, 91, 99-164.

[7] Kolmogorov, A. N. (1941). The Local Structure of Turbulence in Incompressible Viscous Fluid for Very Large Reynolds Numbers. *Mathematical and Physical Sciences*, vol. 434, no. 1890, 1991, pp. 9–13.

[8] François G Schmitt (2007). About Boussinesq's turbulent viscosity hypothesis: historical remarks and a direct evaluation of its validity. *Comptes Rendus Mécanique*, Elsevier Masson, 2007, 335 (9-10), pp.617-627.

[9] Touber, E. and Sandham, N. D. (2008). Oblique Shock Impinging on a Turbulent Boundary Layer : Low-Frequency Mechanisms Mach number. *Fluid Dynamics*, (June):4170–4170.

[10] Touber, E. and Sandham, N. D. (2009). Large-eddy simulation of low-frequency unsteadiness in a turbulent shock-induced separation bubble. *Theoretical and Computational Fluid Dynamics*, 23(2):79–107.

[11] Germano, M., Piomelli, U., Moin, P., and Cabot, W. H. (1991). A dynamic subgrid-scale eddy viscosity model. *Physics of Fluids A*, 3(7):1760–1765.

[12] Nicoud, F. and Ducros, F. (1999). Subgrid-Scale Stress Modelling Based on the Square of the Velocity Gradient Tensor. *Flow, Turbulence and Combustion*, 624:183–200

[13] Kuhn, G. D. (1986). The limiting behaviour of turbulence near a wall. *Journal of Fluid Mechanics.*

[14] Rahman, M., Taghinia, J., Islam, A. K. M. S., Lampinen, M. J., & Siikonen, T. (2015). Modified Norris–Reynolds One–Equation Model. *Procedia Engineering, 105.*

[15] Inagaki, M., Kondoh, T., and Nagano, Y. (2005). A Mixed-Time-Scale SGS Model With Fixed Model-Parameters for Practical LES . *ASME. J. Fluids Eng. January 2005*; 127(1): 1–13.

[16] Morkovin, M. (1962). Effects of compressibility on turbulent flows. *Mécanique de la Turbulence.* A. Favre, pp. 367–380 .

[17] Modesti, D., & Pirozzoli, S. (2016). Reynolds and Mach number effects in compressible turbulent channel flow. *International Journal of Heat and Fluid Flow*, 59, 33–49.

[18] van Driest, E. (1951). Turbulent boundary layer in compressible fluids. *Journal of Aeronautical Sciences* 18, 145–160.

[19] Huang, P. , Coleman, G. , Bradshaw, P. (1995). Compressible turbulent channel flows: DNS results and modeling. *Journal of Fluid Mechanics* 305, 185–218.

[20] Brun, C. , Boiarciuc, M. , Haberkorn, M. , Comte, P. (2008). Large eddy simulation of compressible channel flow. *Theoretical and Computational Fluid Dynamics* 22 (3-4), 189–212 .

[21] Trettel, A., Larsson, J. (2014). Effect of cooling on compressible wall-turbulence. *Proceedings of the 67th Annu. Meet. APS Div. Fluid Dyn.. In: Bull. Am. Phys. Soc.*, Vol. 59 .

[22] Trettel, A., & Larsson, J. (2016). Mean velocity scaling for compressible wall turbulence with heat transfer. *Physics of Fluids*, 28(2).

[23] L. Prandtl (1932). Zur turbulenten Strömung in rohren und längs Platten. *Ergebnisse der Aerodynamischen Versuchsanstalt zu Göttingen* (München Und Berlin, R. Oldenbourg, 1932), Vol. 4, pp. 18–29.

[24] P. Bradshaw (1994). Turbulence: The chief outstanding difficulty of our subject. *Exp. Fluids* 16(3-4), 203–216.

[25] Smits, A. , Dussauge, J.-P. (1996). Turbulent Shear Layers in Supersonic Flow, *2nd edn American Istitute of Physics.*

[26] Pirozzoli, S. (2002). Conservative hybrid compact-WENO schemes for shock-turbulence interaction. *Journal of Computational Physics*, 178(1):81–117.

[27] Gottlieb, S. and Shu, C.-W. (1998). Total variation diminishing Runge-Kutta schemes. *Mathematics of Computation of the American Mathematical Society*, 67(221):73–85.

[28] Pirozzoli, S. (2010). Generalized conservative approximations of split convective derivative operators. Journal of Computational Physics, 229(19):7180–7190.

[29] Yoo, C. S., Wang, Y., Trouvé, A., and Im, H. G. (2007). Characteristic boundary conditions for direct simulations of turbulent counterflow flames. 7830.

[30] Vreman A.W., Kuerten J.G.M. (2014). Comparison of direct numerical simulation databases of turbulent channel flow at $Re_\tau = 180$. *Physics of Fluids*, 26 (1).

[31] Kim, J., Moin, P., & Moser, R. (1987). Turbulence statistics in fully developed channel flow at low Reynolds number. *Journal of Fluid Mechanics*, 177, 133-166.

[32] Kim, John & Mansour, Nagi. (1999). Direct Numerical Simulation of Turbulent Channel Flow up to $Re_\tau = 590$. Physics of Fluids - PHYS FLUIDS. 11. 943-945. 10.1063/1.869966.

[33] Walz, A. (1959). Compressible turbulent boundary layers with heat transfer and pres- sure gradient in flow direction. J. Res. Natl. Bur. Stand. 63, 53–70.

[34] Pirozzoli, S. , Grasso, F. , Gatski, T. (2004). Direct numerical simulation and analysis of a spatially evolving supersonic turbulent boundary layer at M = 2.25. *Phys. Fluids* 16, 530–545.

[35] Duan, L. , Beekman, I. , Martin, M. (2010). Direct numerical simulation of hypersonic turbulent boundary layers. Part 2. Effect of wall temperature. *Journal of Fluid Mechanics* 655, 419–445.

[36] Zhang, Y. , Bi, W. , Hussain, F. , She, Z. (2014). A generalized Reynolds analogy for compressible wall-bounded turbulent flows. *Journal of Fluid Mechanics* 739, 392–420.

[37] De Vanna, F., Picano, F., & Benini, E. (2020). An Immersed Boundary Method for Moving Objects in Compressible Flows. In *ERCOFTAC Series*. https://doi.org/10.1007/978-3-030-42822-8_38.

[38] De Vanna, F., Picano, F., & Benini, E. (2020). A sharp-interface immersed boundary method for moving objects in compressible viscous flows. *Computers and Fluids*. https://doi.org/10.1016/j.compfluid.2019.104415.

[39] Hunt, J., Wray, A, Moin, P. (1988). Eddies, streams, and convergence zones in turbulent flows. *Studying Turbulence Using Numerical Simulation Databases*. -1. 193-208.

[40] Haller, G. (2005). An objective definition of a vortex. *Journal of Fluid Mechanics*, 525, 1-26.

[41] Pope, S. B. (2001). Turbulent Flows. *Measurement Science and Technology*, 12(11), 2020–2021.

[42] Fox D. G., Lilly D. K. (1972). Numerical simulation of turbulent flows. *Rev. Geophys. Space. Phys.* 10:51–72.

[43] Speziale C. G. (1991). Analytical methods for the development of Reynolds-stress closures in turbulence. *Annu. Rev. Fluid Mech.* 23:107– 57.

[44] Lesieur M., Métais O. (1996). New trends in large-eddy simulations of turbulence. *Annu. Rev. Fluid Mech.* 28:45–82.

[45] Moin P. (1997). Progress in large eddy simulation of turbulent flows. *AIAA paper* 97–0749.

[46] Reynolds, O. (1895). On the dynamical theory of incompressible viscous fluids and the determination of the criterion. *Phil. Trans. Roy. Soc. London* A186:123-164.

[47] Launder, B. E., Spalding, D. B. (1974). The numerical computation of turbulent flows. *Comp. Meth. Appl. Mech. Eng.*, 3 (3), pp. 269-289.

[48] Kalitzin, G., Medic, G., Iaccarino, G., Durbin, P. (2005). Near-wall behavior of RANS turbulence models and implications for wall functions, *Journal of Computational Physics*, Volume 204, Issue 1, Pages 265-291.

[49] Pirozzoli, S., & Bernardini, M. (2011). Turbulence in supersonic boundary layers at moderate Reynolds number. *Journal of Fluid Mechanics*, 688, 120-168.

[50] Demetriades, A., Martindale, W. (1983). Experimental determination of one-dimensional spectra in high-speed boundary layers. *Phys. Fluids* 26 (2), 397–403.

[51] Smits, A., Spina, E., Alving, A., Smith, R., Fernando, E., Donovan, J. (1989). A comparison of the turbulence structure of subsonic and supersonic boundary layers. *Phys. Fluids* A 1 (11), 1865–1875.

[52] Spina, E., Smits, A., Robinson, S. (1994). The physics of supersonic turbulent boundary layers. *Annu. Rev. Fluid Mech.* 26, 287–319.

[53] Ganapathisubramani, B., Clemens, N., Dolling, D. (2006). Large-scale motions in a supersonic turbulent boundary layer. *J. Fluid Mech.* 556, 271–282 .